Toward a coherent model for the melting behavior of the deep Earth's mantle

Denis Andrault, Nathalie Bolfan-Casanova, Mohamed Ali M.A. Bouhifd, Asmaa Boujibar, Gaston Garbarino, Geeth Manthilake, Mohamed Mezouard, Julien Monteux, Paraskevas Parisiades, Giacomo Pesce

Toward a coherent model for the melting behavior of the deep Earth's mantle

D. Andrault[1], N. Bolfan-Casanova[1], M.A. Bouhifd[1], A. Boujibar[1], G. Garbarino[2], G. Manthilake[1], M. Mezouar[2], J. Monteux[1], P. Parisiades[2], G. Pesce[1]

[1] Laboratoire Magmas et Volcans, CNRS-OPGC-IRD, Université Clermont Auvergne, Clermont-Ferrand, France
[2] European Synchrotron Radiation Facility, Grenoble, France

Table of contents

1. Abstract

Knowledge of melting properties is critical to predict the nature and the fate of melts produced in the deep mantle. Early in the Earth's history, melting properties controlled the magma ocean crystallization, which potentially induced chemical segregation in distinct reservoirs. Today, partial melting most probably occurs in the lowermost mantle as well as at mid upper-mantle depths, which control important aspects of mantle dynamics, including some types of volcanism. Unfortunately, despite major experimental and theoretical efforts, major controversies remain about several aspects of mantle melting. For example, the liquidus of the mantle was reported (for peridotitic or chondritic-type composition) with a temperature difference of ~1000 K at high mantle depths. Also, the Fe partitioning coefficient ($D_{Fe}^{Bg/melt}$) between bridgmanite (Bg, the major lower mantle mineral) and a melt was reported between ~0.1 and ~0.5, for a mantle depth of ~2000 km. Until now, these uncertainties had prevented the construction of a coherent picture of the melting behavior of the deep mantle.

In this article, we perform a critical review of previous works and develop a coherent, semi-quantitative, model. We first address the melting curve of Bg with the help of original experimental measurements, which yields a constraint on the volume change upon melting (ΔV_m). Secondly, we apply a basic thermodynamical approach to discuss the melting behavior of mineralogical assemblages made of fractions of Bg, $CaSiO_3$-perovskite and (Mg,Fe)O-ferropericlase. Our analysis yields quantitative constraints on the SiO_2-content in the pseudo-eutectic melt and the degree of partial melting (F) as a function of pressure, temperature and mantle composition; For examples, we find that F could be more than 40% at the solidus temperature, except if the presence of volatile elements induces incipient melting. We then discuss the melt buoyancy in a partial molten lower mantle as a function of pressure, F and $D_{Fe}^{Bg/melt}$. In the lower mantle, density inversions (i.e. sinking melts) appear to be restricted to low F values and highest mantle pressures.

The coherent melting model has direct geophysical implications: (i) In the early Earth, the magma ocean crystallization could not occur for a core temperature higher than ~5400 K at the core-mantle boundary (CMB). This temperature corresponds to the melting of pure Bg at 135 GPa. For a mantle composition more realistic than pure Bg, the right CMB temperature for magma ocean crystallization could have been as low as ~4400 K. (ii) There are converging arguments for the formation of a relatively homogeneous mantle after magma ocean crystallization. In particular, we predict the bulk crystallization of a relatively large mantle fraction, when the temperature becomes lower than the pseudo-eutectic temperature. Some chemical segregation could still be possible as a result of some Bg segregation in the lowermost mantle during the first stage of the magma ocean crystallization, and due to a much later descent of very low F, Fe-enriched, melts toward the CMB. (iii) The descent of such melts could still take place today. There formation should to be related to incipient mantle melting due to the presence of volatile elements. Even though, these melts can only be denser than the mantle (at high mantle depths) if the controversial value of $D_{Fe}^{Bg/melt}$ is indeed as low as suggested by some experimental studies. This type of melts could contribute to produce ultra-low seismic velocity anomalies in the lowermost mantle.

2. Introduction

2.1. Melting in the early Earth's mantle

Within the first 100 million years of the Earth's history, the giant Moon forming impact (MFI) melted the Earth almost entirely (Nakajima and Stevenson, 2015). The release of energy induced by the gravitational segregation of the impactor's core could have potentially heated the Earth's core by 3500–4000 degrees above the temperature reached prior to the giant impact (Herzberg et al., 2010; Nakajima and Stevenson, 2015; Rubie et al., 2015). It could have led to a core-mantle boundary (CMB) temperature of the order of 6000 K (Davies et al., 2015; Labrosse, 2015; Nakagawa and Tackley, 2010), well above the mantle solidus of ~4150 K (Andrault et al., 2011; Fiquet et al., 2010). Therefore, the MFI could have caused intensive melting of the mantle at all depths. However, geochemical evidences point out to large scale isotopic heterogeneities that seem to have survived the episode of MFI. For example, the excess in ^{182}W (produced by the decay of ^{182}Hf) measured in 2.7 Ga-old komatiites requires a large-scale magmatic differentiation during the first 30 Ma of the Solar system's history (Touboul et al., 2012). The difference in Xenon isotopic composition between MORBs and the Icelandic plume (Mukhopadhyay, 2012), also indicates two sources with distinct isotopic composition. Finally, geodynamical arguments suggest the presence of an unmixed and primordial material in the deep mantle (Davaille, 1999; Kellogg et al., 1999). Therefore, it is unlikely that primordial mantle temperatures exceeded the liquidus throughout the mantle.

A low viscosity of the magma-ocean is expected to induce vigorous and turbulent convective flow, favoring a homogeneous mixing. In the meantime, heat flux at the magma ocean surface could have been as high as ~10^6 W/m^2, which suggests a very fast crystallization, within ~10^3 years after the MFI (Solomatov, 2007). Longer time scales for cooling are also possible, due to the possible formation of an opaque atmosphere at the Earth's surface preventing heat loss, or other geodynamical complications, such as physical or chemical mantle layering, etc. (Lebrun et al., 2013; Sleep et al., 2014). On the other hand, petrological analyses of Archean and Proterozoic basalts preserved on the Earth's surface show primary magma compositions compatible with mantle potential temperatures (Tp) of only 200-300 degrees higher than today (Herzberg et al., 2010). A similar temperature change is reported between Archean tonalite-trondhjemite-granodiorite associations of 4.0 to 2.5 Ga old (Martin and Moyen, 2002). Such a modest difference of mantle temperature compared to the present situation suggests a relatively rapid mantle cooling just after the MFI.

Finally, it has been suggested that a basal magma ocean (BMO) could have lasted in the lowermost mantle for very long times, billions of years, in correlation with an outer-core temperature significantly higher than the mantle solidus (e.g. (Labrosse, 2015)). This issue remains largely debated, however, because geodynamical models do not explain what could prevent such a hot core from rapid cooling (Monteux et al., 2016; Nakagawa and Tackley, 2010)).

2.2. Evidences for mantle melting today

In the upper mantle, seismic and magneto-telluric profiles present prominent anomalies, in particular at depths between 80 and 200 km (e.g. (Romanowicz, 1995)). Low velocity anomalies have also been reported atop the 410-km mantle discontinuity (Song et al., 2004; Tauzin et al., 2010). Low degree partial melting has often been advocated to explain these anomalies (Revenaugh and Sipkin, 1994), as thermochemical effects alone cannot explain the magnitude of the geophysical anomalies. The possible mechanisms for mantle melting, however, are many. As for the temperature profile, anchor points of the geotherm are provided by phase transformations in major mantle minerals,

typically olivine, the constituent responsible for the seismic discontinuities between 410 and 660 km depths. It yields a potential temperature (Tp) of ~1600 K, which corresponds to the extrapolation to the Earth's surface of the adiabatic temperature profile passing through these anchor points (Katsura et al., 2010). Such a mantle geotherm plots at significantly lower temperatures compared to the melting curve of the peridotitic mantle determined experimentally (Litasov and Ohtani, 2002; Zhang and Herzberg, 1994). Noticeable exceptions exist, for example at mantle ridges, where the adiabatic decompression of the mantle leads to melting in the asthenosphere. On the other hand, in order to invoke melting at higher depths one has to invoke either higher temperatures (such as for OIB, Oceanic Island Basalts), or volatiles that depress the solidus (e.g. (Hirschmann et al., 1999)).

Temperatures in the lowermost mantle depart from the upper mantle geotherm as they are influenced by the heat flux coming from the core at the CMB. A large decrease (>10%) of shear wave velocities is reported in the D''-layer sitting just above the CMB. Even if alternative interpretations are possible, such as a solid-state origin (e.g. Fe-enriched (Mg,Fe)O (Wicks et al., 2010)), it strongly suggests occurrence of partial melting (e.g. (Herzberg et al., 2013; Rost et al., 2005)). Furthermore, the non-ubiquitous character of the seismic features in the D''-layer implies a CMB temperature lower than the mantle solidus. Otherwise, there would be a continuous melting line above the CMB. At the CMB pressure of 135 GPa, the solidus temperature of chondritic and peridotitic mantle was reported to be ~4150 K (Andrault et al., 2011; Fiquet et al., 2010). There, where seismic anomalies appear, mantle partial melting could occur for different reasons: (i) presence of volatile elements, such as in the study of (Nomura et al., 2014) where their pyrolitic composition included ~400 ppm H_2O, which lowered the solidus temperature to ~3570 K. However, we note that a high water content is unlikely in the lower mantle, due to the limited capability of lower mantle minerals to store water below the 660 km discontinuity (Bolfan-Casanova et al., 2003; Panero et al., 2015); (ii) the presence of an excess of silica has been invoked; Indeed, the solidus temperature at the CMB of a mid-ocean ridge basalt, was reported to be 3800 (±150) K, thus significantly lower than for the melting of the average mantle (Andrault et al., 2014). Presence of basalt in the lowermost mantle is supported by seismic tomography imaging deep descent of slabs toward the CMB (e.g. (van der Hilst and Karason, 1999)); (iii) A very large amount of FeO could also lower the melting point of the mantle (Mao et al., 2005). Altogether, the non-ubiquitous seismic features in the D''-layer could very well be correlated to the presence of volatiles, basalt and/or high FeO concentration, together with a CMB temperature of 4100 (±200) K (e.g. (Andrault et al., 2016)).

3. Melting of pure Bridgmanite

3.1. Important bridgmanite properties

MgO becomes extremely refractory with increasing pressure, with a melting point estimated at ~8000 K for a pressure of 135 GPa (Du and Lee, 2014). This contributes in making ferropericlase (Fp) the liquidus phase above 25 GPa, but only up to ~33 GPa, where Bg becomes the liquidus phase for mantle compositions (Ito et al., 2004). The melting curve of Bg dominates the topology of melting diagrams at high mantle depths. The role of Bg is further emphasized by a possible increase of Bg-content with increasing mantle depth, as the comparison between geophysical observations and experiments (e.g. (Murakami et al., 2012; Samuel et al., 2005)) suggest a mantle (Mg+Fe)/Si ratio closer to unity.

Mantle Bg can adopt chemical compositions ranging from (Mg,Fe)SiO_3, produced after decomposition of olivine, to Al-bearing (Mg,Fe)SiO_3, after the high pressure transformation of majoritic garnet below the 660 km discontinuity. A higher compositional variability could also come from the intrinsic high compliance of the Bg crystal structure, which composition can be decomposed in a number of (theoretical) end-members ($MgSiO_3$, $FeSiO_3$, $FeAlO_3$, Al_2O_3, $MgAlO_{2.5}$). It can adopt variable Mg/Si, $Fe^{3+}/\Sigma Fe$, Al/Fe ratios and Fe-content as a function of pressure, temperature, oxygen fugacity, and exchange with ferropericlase. (e.g. (Boujibar et al., 2016; Lauterbach et al., 2000)). The Bg crystal chemistry can thus vary with mantle depth (Andrault et al., 2007) and also laterally if the mantle presents significant heterogeneities. We also remind that the transition pressure from majoritic garnet to Bg increases significantly with the Al-content: compared to pure $MgSiO_3$, an additional 3-4 GPa is required to produce Bg with ~10 wt% Al_2O_3 (Akaogi and Ito, 1999; Irifune et al., 1996).

3.2. Previous studies of bridgmanite melting

In early LH-DAC experiments, visual observations of the sample behavior were used as a major criterion to address the melting of Bg (Figure 1). Two studies performed on $MgSiO_3$ and (Mg,Fe)SiO_3 compositions agree for a steep melting curve above the transition zone pressure, at ~24 GPa (Shen and Lazor, 1995; Zerr and Boehler, 1993). On the other hand, comparison between the melting curves of $MgSiO_3$ and $Mg_3Al_2Si_3O_{12}$ evidences a significant melting temperature depletion, by ~300 K at 40 GPa, due to the presence of Al (Shen and Lazor, 1995). Early works were limited to 60-70 GPa, compared to the 135 GPa prevailing at the CMB. Concerning melting of $MgSiO_3$ in the upper mantle, we note an important curvature of the melting line typical of the lower-density polymorphs (Katsura and Ito, 1990; Presnall and Gasparik, 1990). It can be related to a rapid decrease of the volume of melting (ΔV_m) with increasing pressure and, thus, a relatively high melt compressibility.

Several theoretical works address the equation of state and the melting curve of Bg up to more than 135 GPa, using *ab initio* calculations (Figure 1). The $MgSiO_3$ end-member is generally studied, because such calculations encounter difficulties in addressing the role of transition elements and point defects (such as Al^{3+}, Fe^{3+}, etc.). In all calculations, the initial slope of the melting curve (above ~24 GPa) is relatively steep. This points out to a relatively large volume of $MgSiO_3$-Bg melting, which is dominated by the ~10% volume change at the transition from majoritic garnet to Bg at 660 km-depth (Yu et al., 2011). Based on the propagation of shock waves, $MgSiO_3$ melting was identified at 5000-5500 K for a pressure above 100 GPa (Akins et al., 2004; Mosenfelder et al., 2009). It was also suggested that the volume of Bg melting becomes very small at pressures typical of the lowermost mantle (Mosenfelder et al., 2009; Petitgirard et al., 2015).

3.3. UPDATED MELTING CURVE OF BRIDGMANITE

In this article, we report original measurements of the melting curve of a (Fe,Al)-bearing Bg phase with Fe/(Mg+Fe)=0.12 and Al/Fe=0.9. We acknowledge that this composition corresponds to relatively high Al and Fe contents compared to the expected composition for natural Bg. Experiments were performed using LH-DAC coupled with *in situ* X-ray diffraction on the ID-27 beamline (ESRF, France). All experimental methods are detailed in *Supplementary Materials*. At relatively low pressures, the melting curve of this Bg appears significantly more flat than those reported for pure $MgSiO_3$ (Figure 1). This observation tends to confirm a significant effect of Al on the melting slope, as reported previously between Al-free and Al-bearing starting materials (Shen and Lazor, 1995). We also find that the discontinuous increase of the melting curve slope, related to the majorite to Bg phase transition, is not observed at ~24 GPa, but instead at ~30-35 GPa for this (Fe,Al)-bearing composition. This behavior can be logically related to extension to higher pressures of the garnet stability field in the presence of Al, as described in previous works for Fe-free starting materials (Akaogi and Ito, 1999; Irifune et al., 1996). The relatively lower melting temperature of (Fe,Al)-bearing Bg in the 25-35 GPa pressure range, compared to pure-$MgSiO_3$ and, most importantly, to other lower mantle minerals such as MgO, explains why Bg is not the liquidus phase in this pressure range for typical mantle compositions (Ito et al., 2004).

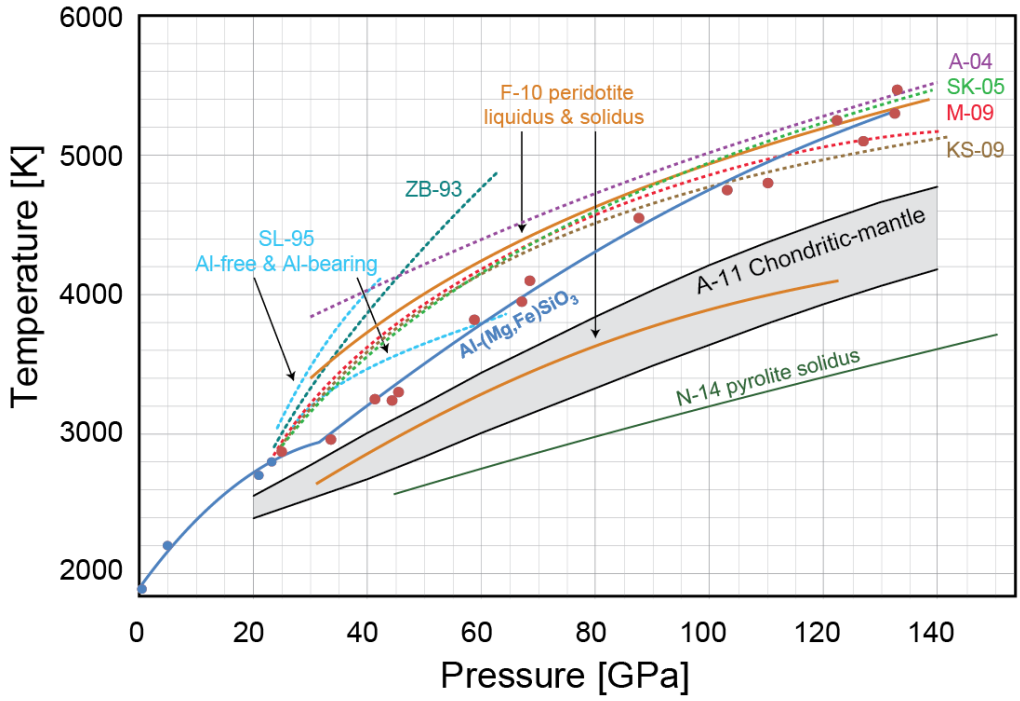

Figure 1: Melting curve of Bg inferred from different experimental and theoretical studies determined using LH-DAC for ($Mg_{0.88}Fe_{0.12}SiO_3$) (Zerr and Boehler, 1993), $MgSiO_3$ and $Mg_3Al_2Si_3O_{12}$ (Shen and Lazor, 1995), shock measurements for $MgSiO_3$ (Akins et al., 2004; Mosenfelder et al., 2009) and *ab initio* calculations for $MgSiO_3$ (e.g. (de Koker and Stixrude, 2009; Stixrude and Karki, 2005)). We also include experimental reports of solidus and liquidus of peridotite (Fiquet et al., 2010), chondritic-type mantle (Andrault et al., 2011) and pyrolite with ~400 ppm H_2O (Nomura et al., 2014). Our new LH-DAC measurements performed from ~24 to ~135 GPa on a (Fe,Al)-rich Bg (red dots and blue guide for the eyes) plot in continuity with previous determinations of mantle melting performed at lower pressures using the large volume press (Blue dots, (Katsura and Ito, 1990; Presnall and Gasparik, 1990)).

At higher pressures, the slope of the (Fe,Al)-bearing Bg melting curve remains fairly constant up to the CMB pressure of 135 GPa, which contrasts with the flattening reported for $MgSiO_3$. This makes the different available results to converge to a temperature of 5100-5500 K for the melting of Bg at the CMB. We remind that the melting curve of $MgSiO_3$-Bg should always plot at higher temperature than that of the (Fe,Al)-bearing composition, due to the incompatible character of Fe and Al. Thus, our experimental determination of the (Fe,Al)-bearing Bg melting curve implies that the melting temperature of $MgSiO_3$-Bg at very high mantle pressures was underestimated by a couple hundred degrees in some previous studies (de Koker and Stixrude, 2009; Mosenfelder et al., 2009). Thus, for further discussions, we will choose the higher melting curve of $MgSiO_3$ Bg as determined from ab initio calculations (Stixrude and Karki, 2005). It can be modeled using a modified Simon and Glatzel equation [$T=T_0\ (P/a + 1)^{1/c}$] with parameters T_0=91 K, a=0.00125 GPa and c=2.83 (Simon and Glatzel, 1929).

We note that the liquidus temperature profile reported previously for peridotite (Fiquet et al., 2010) appears superimposed with the melting curve of $MgSiO_3$-Bg derived from *ab initio* calculations and shock experiments (Figure 1). This is unexpected because (i) the more complex chemical composition of the Bg phase itself, compared to $MgSiO_3$, and (ii) additional Fp and $CaSiO_3$-perovskite (CaPv) phases should both lower the peridotite liquidus below the melting temperature of pure $MgSiO_3$. In their study, (Fiquet et al., 2010) observed large crystals of Bg at the center of the heated spot, where the melting behavior was monitored using *in situ* X-ray diffraction. Chemical composition of Bg grains measured at different locations on a sample synthesized at ~61 GPa show Fe/(Mg+Fe) and Al/Si ratios of ~2.5% and ~8%, respectively. It is possible that their reported measurements of the peridotite liquidus correspond in fact to the melting curve of these large grains of $MgSiO_3$-bearing Bg.

3.4. VOLUME OF BRIDGMANITE MELTING

The dT/dP slope of the Bg melting curve is directly related to the volume (ΔV_m) and entropy (ΔS_m) of Bg melting through the classical Clapeyron relation $dT/dP = \Delta V_m/\Delta S_m$. ΔS_m was reported to be 42.2 J/molK for $MgSiO_3$ at room pressure, based on calorimetric measurements (Stebbins et al., 1984). For melting of $MgSiO_3$ in the stability field of Bg, *ab initio* simulations suggest a ΔS_m value 1.5 times higher (Stixrude et al., 2009). Assuming then a constant ΔS_m value of 63.3 J/molK for melting of (Fe,Al)-bearing Bg at all lower mantle conditions, we now calculate ΔV_m values from the clapeyon slopes of the different melting curves available for Bg (Figure 2a). For the (Fe,Al)-bearing composition, we observe a progressive decrease of $\Delta V_m/V_{Bg}$ (V_{Bg} being the Bg volume) from ~9% to ~5%, when pressure increases from 30 to 140 GPa, respectively. For comparison, earlier studies of the melting behavior of pure $MgSiO_3$ suggest a significantly larger effect of pressure, with $\Delta V_m/V_{Bg}$ varying from 13% at low pressures for some *ab initio* calculations (Stixrude et al., 2009) or even 19% for a shock-wave study (Mosenfelder et al., 2009), to 3-4% at pressures of 135 GPa. The flatter ΔV_m found for the (Fe,Al)-bearing implied by our results is due to a more linear melting curve measured from 30-35 GPa to 135 GPa, compared to pure $MgSiO_3$ (Figure 1). We also show recent measurements of the $MgSiO_3$-glass density performed in the DAC at 300 K up to the CMB pressure (Petitgirard et al., 2015). The $\Delta V_m/V_{Bg}$ recalculated from the later study is significantly lower than all other calculations at high pressures, which should translate into a very flat melting curve. Based on the shadowed region in Figure 2a, we define a most probable range of $\Delta V_m/V_{Bg}$ values decreasing from 11(±2)% to 4(±1)% when pressure is increased from 24 to 140 GPa, respectively.

We also calculated ΔV_m at pressures below 24 GPa using ΔS_m=42.2 J/molK (Stebbins et al., 1984) and using the Clapeyron of melting curves measured in large volume press (LVP) experiments. We note that the final interpretation of ΔV_m can be complicated by the occurrence of four different $MgSiO_3$ polymorphs between 1 bar and 24 GPa (Presnall, 1995). In particular, the Clapeyron slope of majorite melting remains largely uncertain, due to a limited pressure range available. For this reason, we modeled the $MgSiO_3$ melting line using a 2nd degree polynomial regression across the whole pressure range from 0 to 24 GPa. The calculated $\Delta V_m/V_{Bg}$ decreases strongly with increasing pressure converging to 1% at ~24 GPa (Figure 2a). It makes a volume change of ~8% at the majorite to Bg transition for the (Fe,Al)-bearing composition of our study, or ~10% in average for the most probable range of $\Delta V_m/V_{Bg}$ that we have defined above, both values agreeing well with the ~10% suggested previously for $MgSiO_3$ (Yu et al., 2011).

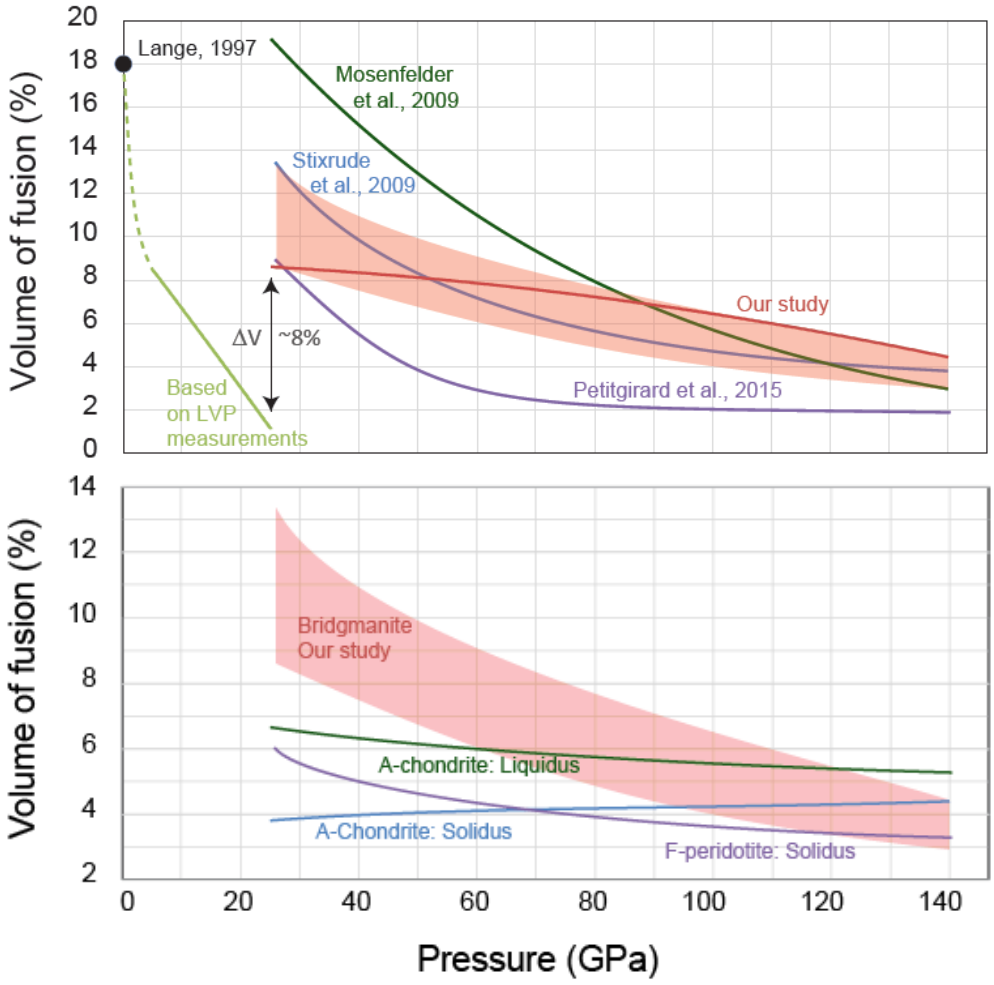

Figure 2: (a) Volume of melting ($\Delta V_m = V_{melt}-V_{Solid}/V_{Bg}$, where V_{Bg} is volume of Bridgmanite) derived from the melting curve of Bg (Figure 1) with various $(Mg,Fe)(Si,Al)O_3$ compositions We also report the value of 18% measured for pure $MgSiO_3$ at 1 bar (Lange, 1997) and $\Delta V_m/V_{Bg}$ recalculated from density measurements of $MgSiO_3$-glass in a DAC (Petitgirard et al., 2015). Shadowed pink region is the most probable range of mantle $\Delta V_m/V_{Bg}$ values. (b) ΔV_m derived from the solidus and/or liquidus profiles of the A-chondritic (Andrault et al., 2011) and F-peridotitic (Fiquet et al., 2010) models of mantle melting. ΔV_m is calculated using the Clapeyron relation. Calculation of $\Delta V_m/V_{Bg}$ along solidus and liquidus profiles assume an ideal mixing model to estimate the melt entropy (see text).

4. MELTING DIAGRAMS FOR TYPICAL LOWER MANTLE MATERIALS

4.1. EXPERIMENTAL DETERMINATION OF THE MELTING BEHAVIOR

Studying experimentally phase relations in a partially molten geological material under P-T conditions of the Earth's interior remains a challenging task. The use of LVP facilitates largely the chemical analysis of coexisting phases in recovered samples, compared to LH-DAC. For example, melting behavior of fertile peridotite and CI chondritic mantle were documented up to ~35 GPa (Ito et al., 2004). It was demonstrated that the liquidus phase changes from Fp to Bg at about 33 GPa, a situation that was confirmed later by LH-DAC experiments (Andrault et al., 2011; Fiquet et al., 2010). However, LVP samples (and *a fortiori* LH-DAC samples) synthesized at lower mantle conditions always encounter relatively large temperature gradients, which yields heterogeneous microstructure and chemical zoning. In such cases, the sequence of phase disappearance from solidus to liquidus temperatures is usually retrieved from the position of phases relative to the temperature gradient. Still, this procedure prevents the precise determination of the equilibrium solid-liquid partition coefficients.

When coupled with *in situ* X-ray diffraction, LH-DAC is well suited to determine melting curves of various geological materials, because the available temperature range extends up to more than 6000 K (Suppl. Figure 1). Melting criteria are generally based on the disappearance of diffraction peaks and phase(s), which corresponds in fact to the determination of a pseudo-eutectic temperature (PET). Recently, PET of peridotite (Fiquet et al., 2010), chondritic-mantle (Andrault et al., 2011) and pyrolite (Nomura et al., 2014) was reported with substantially different values. Disagreements cannot be reconciled based on the moderate compositional variations between starting materials, among which the major difference lies in the Bg/(Bg+CaPv+Fp) ratio from 0.59, 0.63 and 0.75 for peridotite, pyrolite and chondritic mantle, respectively. Studies using peridotitic (F-peridotitic model) and chondritic (A-chondritic model) starting materials show similar solidus evolution as a function of pressure, pointing out to a PET of 4150±150 K at the CMB. The lower value reported in the study using pyrolite could be due to a more precise determination of the solidus, thanks to the use of 3D X-ray tomography, but more likely because of the presence of 400 ppm H_2O in their sample that triggers melting (Nomura et al., 2014).

4.2. PSEUDO-EUTECTIC TYPE MELTING IN THE DEEP MANTLE?

The melting diagram between the three lower mantle phases (Bg, CaPv and Fp) presents an eutectic behavior (e.g. (de Koker et al., 2013; Liebske et al., 2005; Liebske and Frost, 2012)), which implies (i) a PET and (ii) a melt composition at the PET located within the ternary diagram. The PET and the melt composition should be independent of the Bg, CaPv and Fp molar fractions in the bulk material, as long as the chemical compositions of these three phases do not vary significantly. A major issue for geological materials is that the onset of melting (the solidus) can possibly occur at a temperature lower than the PET. In such a case, a melt appears without disappearance of a phase from the mineral assemblage. This can happen when the solubility limit of an incompatible element is overpassed at a given condition of pressure and temperature. This behavior has not been reported yet for any mantle compositions under the P-T conditions typical of the lower mantle. In contrast, available LH-DAC experiments report disappearance of one phase at the onset of melting (see above). Also, chemical analyses of melts obtained after partial melting of peridotite at ~24 GPa show compositions close to the starting material (e.g. with a relatively lower MgO/SiO_2 ratio (Tronnes and Frost, 2002)), which is incompatible with incipient mantle melting.

Above the solidus temperature, partition coefficients between Bg or CaPv and the melt ($D_i^{Solid/melt}$) were investigated experimentally for many elements. Except for a very few of them (such as Li and Ba), $D_i^{Solid/melt}$ values are found to lie above 3.10^{-1}, which corresponds to a moderately incompatible behavior (Corgne et al., 2005). These results suggests that the minor elements may not reach their solubility limit easily. Of course, volatiles such as H_2O (but also CO_2) are well known to depress the solidus and potentially favor incipient mantle melting. We note, however, that (i) carbonate phases may be relatively refractory in the lower mantle (Thomson et al., 2014) and (ii) a high water content in the lower mantle is unlikely, due to limited capability of the lower mantle minerals to store water below the 660 km discontinuity (Bolfan-Casanova et al., 2003). Thus, even if water has an effect of the solidus of the lower mantle it does not mean that water is actually present. In summary, experimental evidences strongly suggest a moderate temperature difference between solidus and PET, if any.

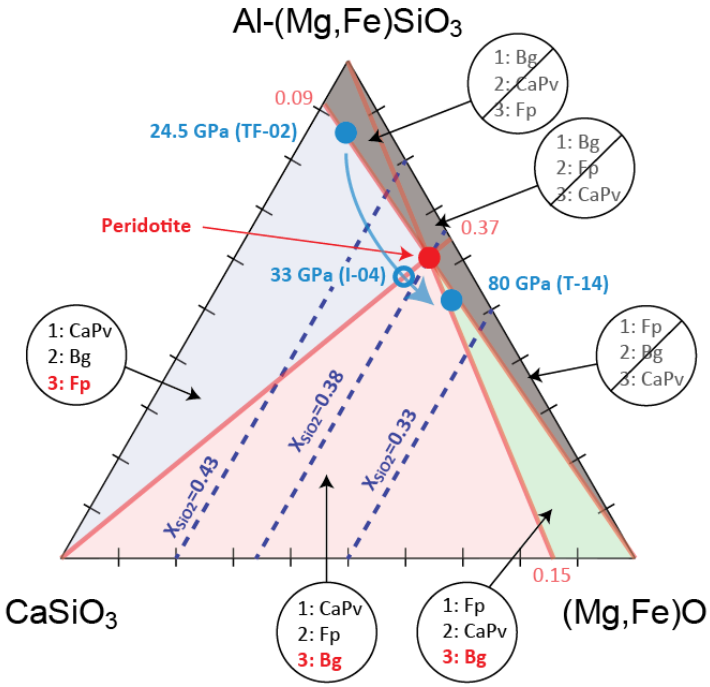

Figure 3: Ternary diagram between Bg, Fp and CaPv, the three major phases in the lower mantle. Due to its eutectic shape, melt compositions should always plot within this diagram. The Red dot and lines correspond to the peridotitic composition and its associated Fp/Bg, CaPv/Bg and CaPv/Fp ratios. Blue dots are melt compositions determined experimentally (Ito et al., 2004; Tateno et al., 2014; Tronnes and Frost, 2002). The blue arrow shows the change in melt composition with pressure. In each colored region of the ternary diagram, the expected sequence of phase disappearance upon melting are reported inside circles: 1, 2 and 3 are solidus, intermediate and liquidus phases, respectively.

4.3. SEQUENCE OF PHASE DISAPPEARANCE UPON MELTING

In the ternary diagram between Bg, CaPv and Fp, the difference in composition between the bulk composition and the melt defines the sequence of phase disappearance upon melting. For example, melting of peridotite would likely induce a melting sequence from CaPv (at solidus), Bg to Fp (at liquidus), if the PE-melt would present significantly higher $CaSiO_3$-content and lower (Mg,Fe)O-content, compared to peridotite. Thus, the ternary diagram can be divided into six different regions where the melting sequence should be different, depending on the PE-melt composition (Figure 3).

Composition of melts relevant to deep mantle partial melting were reported after experiments performed at 24.5 GPa using LVP (Tronnes and Frost, 2002) and 80 GPa using LH-DAC (Tateno et al., 2014). Despite the fact that these melts may differ from PE-melts, if experimental temperatures have been higher than PET, they provide precious anchors for melt compositions in the ternary diagram. Composition of these two melts (corresponding to 24.5 and 80 GPa) plot on each side of the Fp/Bg ratio of 0.37, which corresponds to the peridotite composition. This observation is compatible with a third experimental anchor point where the liquidus phase has changed from Fp to Bg at about

~33 GPa for a fertile peridotite (Ito et al., 2004). Thus, the melt composition evolves toward higher (Mg,Fe)O-contents with increasing pressure.

Another important observation is the melt composition at 80 GPa, which presents a CaPv/Fp ratio very close to the peridotitic value of 0.15. It suggests that both phases, CaPv and Fp, disappear almost simultaneously at the PET upon partial melting of peridotite in the deep lower mantle. In this work, we make the assumption that CaPv and Fp disappear simultaneously at the PET at lower mantle pressures. This assumption is not severe. If Fp would disappear first, negligible amount of CaPv would remain. Indeed, the total amount of CaPv is below ~6 mol% for compositions relevant to the deep mantle. In the case where CaPv would disappear first, higher Fp content could theoretically remain after melting at the PET. Indeed, Fp is found at a level of 19, 32 or 35 mol%, for chondritic, pyrolitic or peridotitic compositions, respectively. However, the molar volume of Fp is twice less than those of Bg and CaPv. Also, it is likely that the melt dissolves a significant part of Fp at the PET (Tateno et al., 2014; Tronnes and Frost, 2002), which should yield to a low Fp-content in the residual solid.

4.4. Liquidus temperatures and Bg-content in melts

The melting behavior can be modeled at various mantle pressures (for example 40 GPa, 80 GPa and 135 GPa) using (pseudo) binary phase diagrams, where one end-member is Bg, the liquidus phase, and the other is the sum of all the other chemical components (Figure 4). We prefer to use Fe-free Bg as an end-member, instead of (Fe,Al)-bearing Bg, due to the preferential partition of Fe to the melt (this matter is discussed later in the article). Still, we consider an Al-bearing Bg end-member, because the Al-behavior upon partial melting remains poorly constrained. Compositional axis of such binary diagram is thus the molar fraction of Fe-free Bg. Melts include Fp, CaPv, (virtual) $FeSiO_3$-Bg and a fraction of Fe-free Bg end-members. Peridotitic and chondritic mantle, as well as our (Fe,Al)-bearing Bg composition plot at 59, 75 and 88 mol% of Fe-free Bg, respectively. For the PET, the A-chondritic model indicate “solidus” temperatures of 2690, 3340 and 4130 K at pressures of 40, 80 and 135 GPa, respectively (Andrault et al., 2011). For the Fe-free Bg end-member, we use ab initio calculations for $MgSiO_3$-Bg (Stixrude and Karki, 2005), as discussed above. Two LH-DAC studies report liquidus temperatures of A-chondritic and F-peridotitic models (Andrault et al., 2011; Fiquet et al., 2010). Finally, the independent reports of the Bg-content in melts (i) measured after partial melting of pyrolite (Tateno et al., 2014) and (ii) calculated in the $MgSiO_3$-MgO system (de Koker et al., 2013; Liebske and Frost, 2012) are also shown. We note that the two later studies did not included the CaPv component, which could numerically yield an overestimation of the Bg-content in the melt.

At each selected mantle pressure, we draw lines from the melting temperature of the Bg end-member, through the liquidus temperature of the A-chondritic model, toward the PET (Figure 4). These lines provide estimates of liquidus temperatures as a function of the bulk mantle composition. In addition, intersections between these lines and PET provide estimates of the Bg-content in PE-melts, as a function of pressure. Uncertainties arise from (i) controversial reports of the Bg melting temperature as a function of pressure (Figure 1) and (ii) unknown curvature of the liquidus profile in these diagrams. Consequently, we colored in pink regions where the presence of liquidus is the most probable. We excluded from colored regions (i) PE-melts with a fraction of Fe-free Bg higher than peridotite, because it would be contradictory with Bg becoming the liquidus phase above ~33 GPa (Ito et al., 2004), (ii) a previous study reporting inaccurate Bg melting curve at low pressures (Akins et al., 2004) and (iii) trends extrapolated from (de Koker and Stixrude, 2009; Mosenfelder et al., 2009) as they may have underestimated the Bg melting temperature by a couple hundred degrees in the

lowermost mantle (see text associated to Figure 1). We note that our method is not appropriate to pressures lower than ~33 GPa, when Bg is not the liquidus phase.

Based on the width of the regions of confidence, the liquidus temperatures appears to be constrained within ±150 K at all mantle pressure, temperature and compositions. An uncertainty to which we should still add a similar value associated to the experimental error in the determination of PET and Bg melting temperature. On the other hand, uncertainty in Bg-content in PE-melt and along liquidus lines is about ±5%. The Bg-content in the PE-melt appears almost independent of lower mantle pressure at 55(±5) mol%. With increasing temperature above PET, the Bg-content in melt should logically increase until it reaches the bulk mantle composition. Altogether, these binary melting diagrams can be numerically constrained by three parameters: (i) a constant Bg-content of 55(±5) mol% in PE-melt, and two modified Simon and Glatzel (SG) equations [$T(P)=T_0\ (P/a+1)^{1/c}$] with parameters (ii) T_0=2045 K, a=92 GPa and c=1.3 for the PET (Andrault et al., 2011) and (iii) T_0=91 K, a=0.00125 GPa and c=2.83 for the Bg end-member ((Stixrude and Karki, 2005), see above). Then, liquidus temperatures between PE-melt and Bg can be defined as a function of pressure and mantle composition using:

$$T^{Liq}_{Mantle}(P,X_{Bg}^{Mantle})= SG(Bg)-[(SG(Bg)-SG(PEM))*(1-X_{Bg}^{Mantle})/(1-X_{Bg}^{PEM})]$$

where SG(PEM) and SG(Bg) are PE-melt and Bg melting temperatures, respectively, calculated at a target mantle pressure (P) using SG equations. X_{Bg}^{PEM} and X_{Bg}^{Mantle} are Bg mole fractions in the PE-melt (fixed at 55 mol%) and the bulk mantle, respectively.

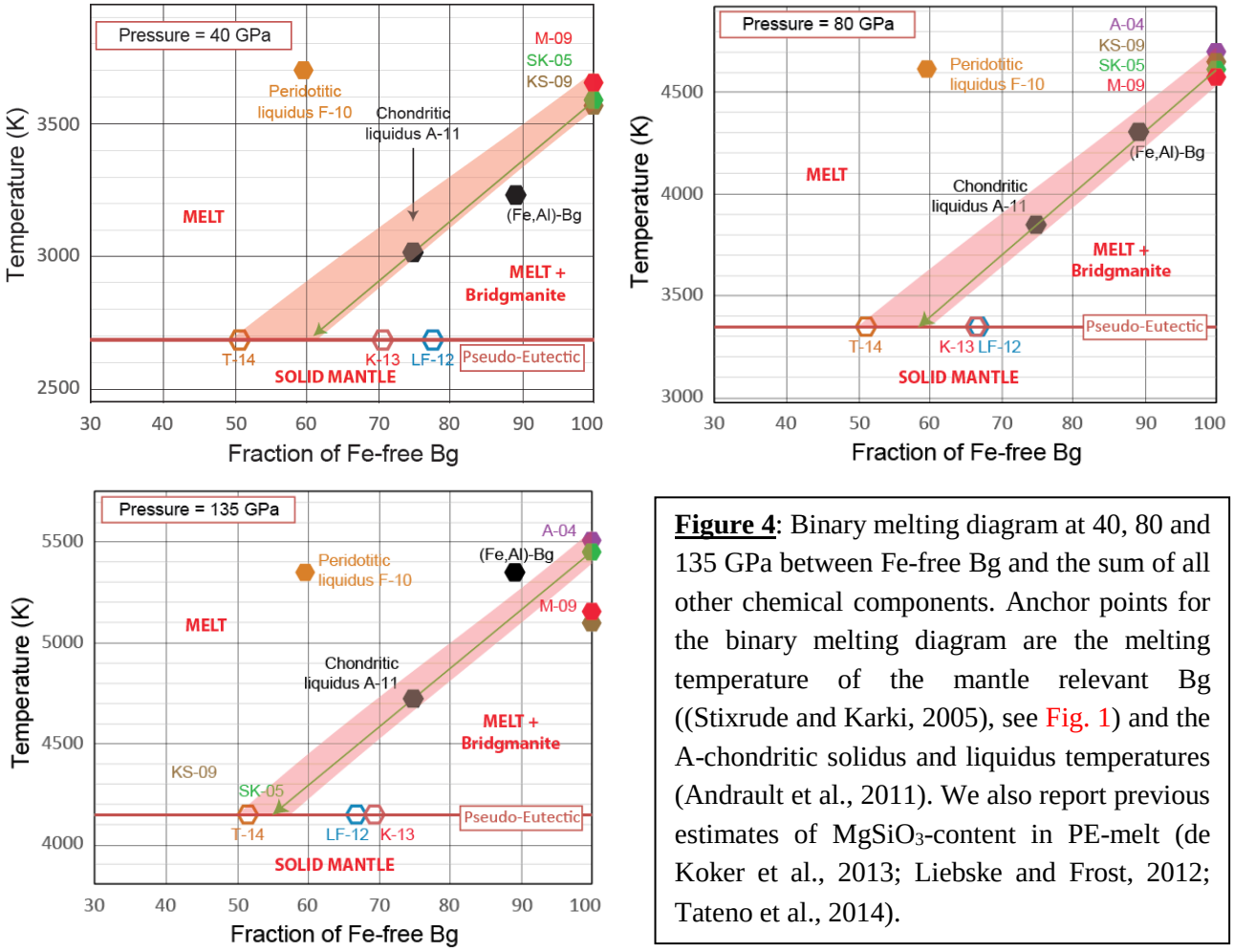

Figure 4: Binary melting diagram at 40, 80 and 135 GPa between Fe-free Bg and the sum of all other chemical components. Anchor points for the binary melting diagram are the melting temperature of the mantle relevant Bg ((Stixrude and Karki, 2005), see Fig. 1) and the A-chondritic solidus and liquidus temperatures (Andrault et al., 2011). We also report previous estimates of $MgSiO_3$-content in PE-melt (de Koker et al., 2013; Liebske and Frost, 2012; Tateno et al., 2014).

For a peridotitic mantle composition, binary phase diagrams suggest a difference of less than 300 K between PET and liquidus at all lower mantle pressures. This is in very good agreement with the value of 250 K proposed based on a thermodynamic melting model (Liebske and Frost, 2012). The

difference between the PET and the liquidus increases for larger fractions of Bg in the bulk material, and in a primitive chondritic mantle it can reach up to 500 degrees. This confirms the wide range of mantle depths where partial melting should have occurred in the framework of an early magma ocean (e.g. (Kojitani and Akaogi, 1997; Miller et al., 1991)).

4.5. SiO_2 CONTENT IN PSEUDO-EUTECTIC MELTS

Another parameter controlling the melt properties is its SiO_2-content ($X(SiO_2)$). It can be derived directly from Figure 4, by converting the amount of Fe-free Bg in the melt into its SiO_2 contribution. Based on our primary assumption that Fp and CaPv dissolve concomitantly in the melt at the PET, the SiO_2-content of the CaPv component is also added to the melt composition. This calculation can be performed for all types of melt along liquidii, as long as pressure is above ~33 GPa. Still, we only discuss here the composition of PE-melts. We actually translate into $X(SiO_2)$ the regions of confidence defined above for Bg-contents in PE-melts (Figure 5). Independent values of $X(SiO_2)$ in lower mantle melts were reported previously based on *ab initio* calculations (de Koker et al., 2013), thermodynamic modeling of LVP experiments (Liebske and Frost, 2012) and chemical analyses of LH-DAC samples (Nomura et al., 2011; Tateno et al., 2014). At about ~33 GPa, the change of liquidus phase from Fp to Bg reported upon peridotite melting suggests that $X(SiO_2)$ in the melt crosses the peridotitic value of 38.3% (Ito et al., 2004).

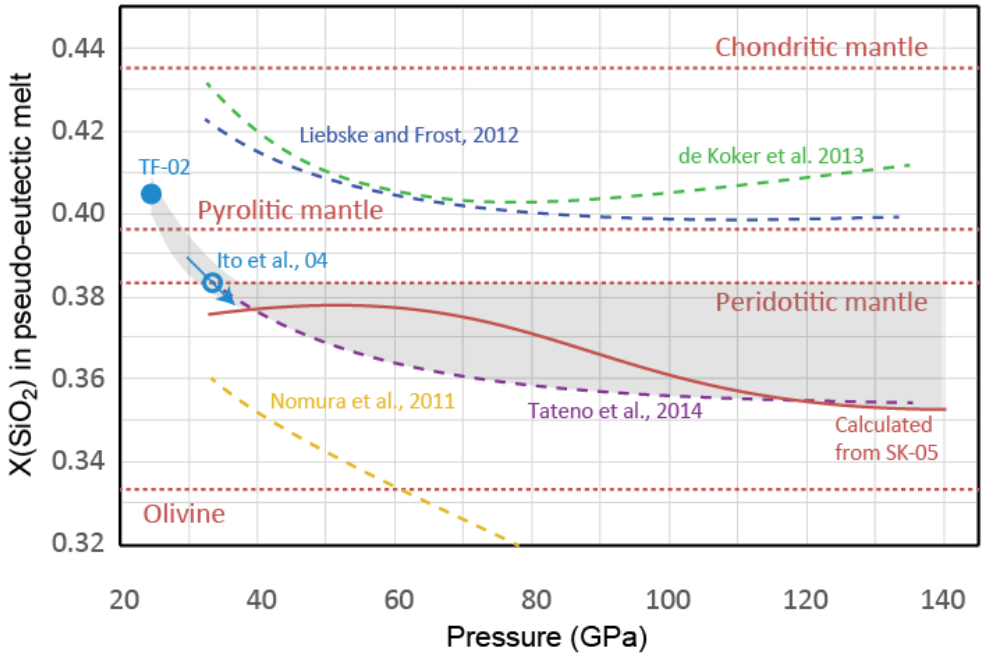

Figure 5: Pressure change of the SiO_2-content in pseudo-eutectic melt. Horizontal dotted lines are $X(SiO_2)$ typical of olivine, peridotite, pyrolite and chondritic-mantle. The red line is derived from the Bg melting curve (Stixrude and Karki, 2005) associated with the thermodynamical treatment elaborated for the discussion of Figure 4. Dashed lines represent previous calculations (de Koker et al., 2013; Liebske and Frost, 2012) or the experimental determination (Tateno et al., 2014) of $X(SiO_2)$ in melts. The shaded gray area corresponds to the most likely $X(SiO_2)$ of lower mantle melts.

The melt $X(SiO_2)$ likely remains significantly lower than 0.40 at higher pressures in the lower mantle, because Bg was broadly reported to be at the liquidus for pyrolite (Nomura et al., 2014) and peridotite (Fiquet et al., 2010). The fact that two models (de Koker et al., 2013; Liebske and Frost, 2012) propose higher $X(SiO_2)$ could be related to calculations restricted to the $MgSiO_3$-MgO system. The difference between the simple MgO-SiO_2 system and the mantle-related compositions suggests that Ca and Fe should enter the melt preferentially as CaO and FeO, rather than $CaSiO_3$ and $FeSiO_3$,

thus lowering $X(SiO_2)$. Such behavior translates into a significantly stronger incompatible character of Ca and Fe, compared to Mg and Si (Liebske et al., 2005), which is already well known for low-pressure melting. The range of possible melt $X(SiO_2)$ appears to extend between the peridotite and chemical analyses performed on LH-DAC samples (Tateno et al., 2014). It corresponds to an almost fixed $X(SiO_2)$ value of 37.0% (±1.5%). This most probable range of $X(SiO_2)$ plots in good continuity with data reported at lower pressure based on LVP experiments (Ito et al., 2004; Tronnes and Frost, 2002). In summary, deep PE-melts appear to adopt a composition only slightly enriched in Fp compared to peridotite, if any.

4.6. DEGREE OF PARTIAL MELTING AT PSEUDO-EUTECTIC TEMPERATURES

We can now calculate the expected degree of partial melting (F) at the PET for peridotitic, pyrolitic and chondritic mantle compositions, based on our estimation of deep-mantle melt compositions (Figures 4 and 5). F (in vol%) at PET can be estimated using the molar volumes for Bg, Fp and CaPv (Equations of state needed to take into account the effect of pressure and temperature on volumes are described below). Logically, the calculated F value at PET varies with the difference in composition between the PE-melt and the bulk material. The closest the mantle composition is from the melt, the highest F value is expected at the PET. Calculated ranges of possible F values at PET appear to be more than 83, 74 and 46 vol%, for peridotitic, pyrolitic and chondritic mantle compositions, respectively (Figure 6).

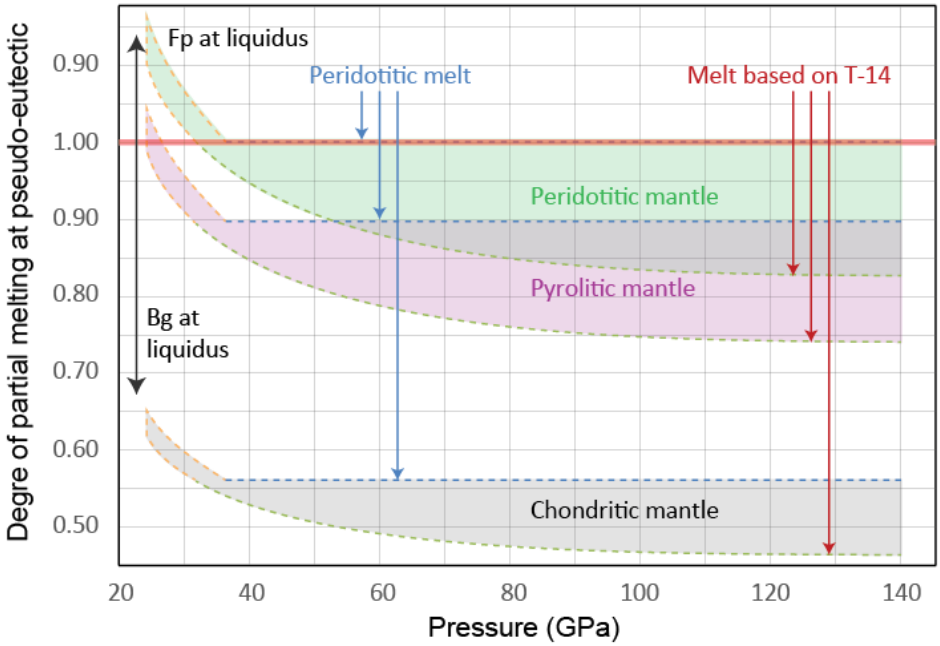

Figure 6: Degrees of mantle partial melting (vol%) expected at pseudo-eutectic temperature (PET) in the lower mantle under the assumptions that CaPv and Fp phases disappear jointly upon melting. Degrees of partial melting are calculated for typical chondritic, pyrolitic and peridotitic mantle compositions, based on the possible range of PE-melt composition refined in Figure 5. T-14 stands for (Tateno et al., 2014).

We note that a similar conclusion was reached previously (e.g. (Herzberg and Zhang, 1998)) based on the residual harzburgite signature of most komatiites with Cretaceous and late-Archaean ages, which can be interpreted to have formed by about 25 to 60% anhydrous melting of mantle peridotite in hot plumes.

The melting relations discussed above have implications for our understanding of the melting in the deep mantle today. For example, in the ultra-low velocity zones (ULVZ) just above the CMB, the

high F values determined for PET imply that the ULVZ cannot correspond to partial melting of the average mantle, because the degree of partial melting in the ULVZ as inferred by seismology is much lower than the threshold value of 46%. But a lower F-value could be achieved (i) for a locally high concentration in volatile elements, which would favor incipient mantle melting below the PET or (ii) for another type of geological material, such as subducted basalts (Andrault et al., 2014).

5. MELT BUOYANCY IN THE DEEP MANTLE

5.1. MAJOR PARAMETERS CONTROLLING THE MELT BUOYANCY

Dynamical behavior of a partially molten mantle is largely affected by the density contrast between the melt and the solid fractions ($\Delta\rho_{m\text{-}s}=(\rho_m-\rho_s)/\rho_s$). While melt buoyancy plays a major role in chemical segregation and planetary differentiation, the fact that its sign is positive or negative produces two different geodynamical situations. Melt buoyancy can also vary with mantle depth, due to (i) a possible change of the melt composition and (ii) different PVT equations of state for the melt and the mantle residue. In the present-day mantle, ascent, or descent, of some melts could contribute to surface volcanism, or accumulation of melts in the lowermost mantle, respectively. In a crystallizing magma ocean, it is classically accepted that crystals would settle, compact and reject the melt toward the Earth's surface (Boukare et al., 2015; Solomatov, 2007). However, this question became much debated after it was proposed that an early basal magma ocean could be produced by dense melts stored above the CMB (Labrosse et al., 2007; Nomura et al., 2011). Solid-liquid density inversions are not unusual. Many years ago, it was already proposed that basaltic and komatiitic magmas would become denser than olivine and garnet at depths of 245-500 km (Agee, 1998).

Major parameters controlling the buoyancy of deep-mantle melts are (i) changes in atomic packing between solid and liquid phases, which most generally produces a positive volume of melting (ΔV_m), (ii) Fe partition coefficient between the solid residue and the melt ($D_{Fe}^{Bg/melt}$), because Fe is the heaviest major element, and (iii) MgO/SiO_2 ratio in the melt, because SiO_2-based atomic packing presents a relatively high bulk modulus. We chose to use $D_{Fe}^{Bg/melt}$ ($D=X_{Fe}^{Bg}/X_{Fe}^{melt}$, with X being the molar fraction), rather than the distribution coefficient $K_{Fe}^{Bg/melt}$ ($K=(X_{Fe}/X_{Mg})^{Bg}/(X_{Fe}/X_{Mg})^{melt}$), because X_{Mg}^{melt} can vary with pressure, temperature and bulk composition independently from X_{Fe}^{melt}. Nothing prevents X_{Mg}^{melt} and X_{Fe}^{melt} to vary in a correlated way, which would contradict the proper definition of K.

Concerning the volume difference between solids and melts, both phases undergo (i) volume changes upon P and T according to their respective equation of state and (ii) a number of structural transformations with increasing mantle depth. In the solid state, equation of states of major mantle minerals are relatively well constrained (Matas et al., 2007). Structural transformations in the melt are much more progressive than in the solid, but can still contribute to a net increase of the melt density with increasing mantle depths. Due to the disordered and time-dependent nature of the melt structure, each structural entity has a finite lifetime. And when pressure is applied, structural entities can progressively evolve. In polymerized liquids, polyhedral chains can bend, eventually break and recompose differently (Stolper and Ahrens, 1987; Wang et al., 2014). All major cations progressively change their coordination shell (Bajgain et al., 2015) to allow compaction of the oxygen sub-lattice (Zeidler et al., 2014). The major change is probably Si, which progressively changes coordination number from four-fold to six-fold between ~20 to ~40 GPa (Benmore et al., 2010; Guillot and Sator, 2007; Sanloup et al., 2013; Sato and Funamori, 2010). These progressive transformations yield a room pressure bulk modulus significantly lower for the melt than for the crystalline counterpart. However, the pressure derivative of the bulk modulus is generally much higher, due to the progressive loss of some compaction mechanisms, after major voids have disappeared from the melt structure at moderate pressures.

At shallow mantle depths, while the melt structure has already undergone significant compaction, major mantle minerals, in particular olivine, have not yet transformed to a denser polymorph. For this reason, there could be a neutral melt buoyancy, or even a positive $\Delta\rho_{m\text{-}s}$ (i.e. a sinking melt), at mantle depths just above the 410 km discontinuity (Matsukage et al., 2005; Sakamaki et al., 2006). It could produce a kind of density trap, where melts produced above and below would accumulate and remain gravitationally stable in this mantle region (e.g. (Lee et al., 2010)). At lower mantle pressures, a previous study tentatively addresses $\Delta\rho_{m\text{-}s}$ for a number of melt and solid compositions (Figure 7; (Funamori and Sato, 2010), see also (Thomas et al., 2012)). Reporting in this diagram our estimates of $X(SiO_2)$ in PE-melt retrieved from Figure 5 narrows down the range of possible silica contents between ~35.2 to ~38.3 mol%. We note that the SiO_2-content in the melt should increase with increasing temperature above the PET, because the PE-melt is relatively depleted in SiO_2 compared to the mantle composition. Ultimately, the melt and the bulk mantle become similar at the liquidus temperature, when the solid residue disappears completely. Altogether, the rather limited range of possible SiO_2-content in mantle melts points out to the fact that the less constrained parameters needed to address melt buoyancy at mantle depths are ΔV_m, the volume of melting, and $D_{Fe}^{Bg/melt}$, the Fe solid-liquid partitioning.

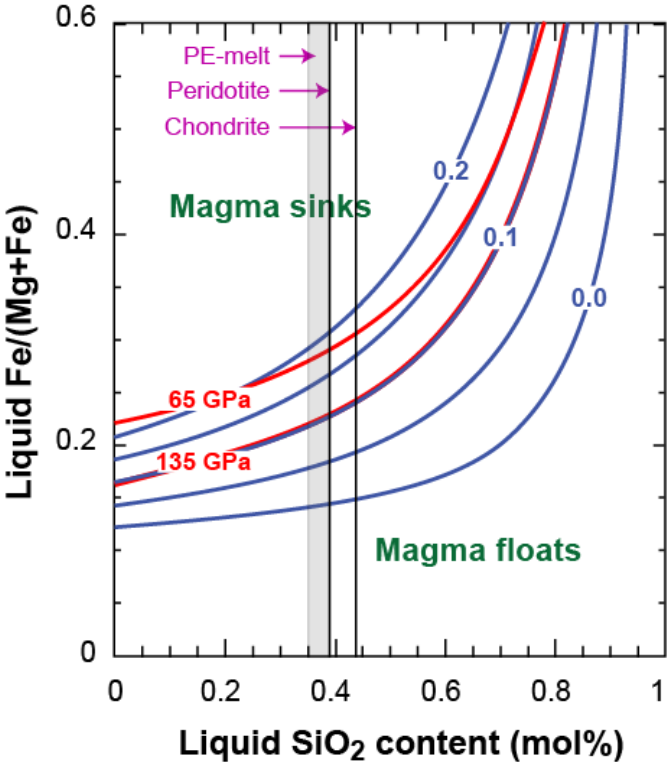

Figure 7: Relative buoyancy between mantle melts of various compositions and (i) the $(Mg,Fe)SiO_3$ Bg with Fe-contents of 0, 10, or 20% (blue lines) and (ii) the lower mantle at pressures of 65 and 135 GPa (red lines). Along each blue or red lines, the melt and the given solid phase (Bg or lower mantle) have the same density. Higher SiO_2-content or lower Fe/(Mg+Fe) ratio, compared to a given line, yield melts buoyant compared to the solid phase considered. The gray region corresponds to the likely SiO_2-content in PET-melts in the mantle (see Figure 5). SiO_2-content values for chondritic and peridotitic mantle are also reported. This Figure is modified from (Funamori and Sato, 2010).

5.2. VOLUME OF MANTLE MELTING

While the ΔV_m corresponding to the melting of a pure phase, such as Bg, can be estimated based on its melting curve (Figure 2a), the volume of melting becomes more difficult to address in the case of the partial melting of the mantle between its solidus and liquidus. In addition, the equation of state of the melt changes significantly with its composition (de Koker et al., 2013; Thomas and Asimow, 2013). For example, Mg_2SiO_4-liquid becomes denser than lower mantle phases at pressures above ~40 GPa, while $MgSiO_3$-liquid remains buoyant at all mantle pressures (Thomas and Asimow, 2013). Thus, assuming a simplified melt composition, such as $MgSiO_3$, may not be much relevant for discussing the buoyancy of natural melts in the deep mantle. A more realistic exercise is to estimate the real density difference between the solid residue and a melt of relevant composition in the Bg-CaPv-Fp system. The solid residue can be a simple phase (Bg, or Fp below ~33 GPa), or a typical

mantle composition (e.g. pyrolite), which would be relevant to model melt buoyancy in the context of an early crystallizing magma ocean (high F), or partial melting in the present-day lower mantle (low F), respectively. The melt composition at various P and T can be derived from melting diagrams (Figure 4).

In Figures 2b, we intend to use the slopes of solidus and liquidus reported for mantle melting from LH-DAC experiments (Andrault et al., 2011; Fiquet et al., 2010) to retrieve thermodynamical information relevant to melts. We compare the solidus, or liquidus, profile to a Clapeyron slope which would record melting of the first fraction of solid mantle, or the last fraction of Bg, respectively. At the solidus temperature, the entropy of melting (ΔS_m) can be estimated from the sum of melting entropies of each phase present in the melt, plus a mixing entropy. We used ΔS^i_m values of 63.3, 63.3 and 13.0 J/molK for the melting entropy of Bg (Stixrude et al., 2009), CaPv (similar to Bg) and Fp, respectively. We note that the room pressure value of ΔS^{MgO}_m was reported to be significantly larger than that of Fp, at ~35 J/molK, however, it decreases rapidly with increasing pressure to 25 GPa (Vocadlo and Price, 1996). Composition of the PE-melt is considered to be 60% Bg, 30% Fp and 10% CaPv, in agreement with Figures 3 and 4. However, changing the phase contents does not affect greatly the calculated ΔS_m value of ~55 J/molK. At the liquidus temperature, we assume that the ΔS_m of the bulk rock is similar to that of Bg, neglecting the fact that the melt in which last grains of Bg get dissolved has a composition slightly different from Bg. Based on these assumptions, we calculate volumes of melting at solidus and liquidus, using the Clapeyron equation (Figure 2b).

For the A-chondritic model, the values of $\Delta V_m/V_{Bg}$ at the solidus and at the liquidus appear almost independent of mantle pressure, at values of 4(±1)% and 6(±1)%, respectively. The $\Delta V_m/V_{Bg}$ at the solidus of the F-peridotitic model plots at similar values, however, due to a larger curvature in the melting curve, its associated $\Delta V_m/V_{Bg}$ varies more with pressure. We note that if we would have included a supplementary non-ideal mixing contribution to ΔS_m (de Koker et al., 2013), the $\Delta V_m/V_{Bg}$ values would have been ~0.5 % higher. Calculations appear compatible with a small variation of the volume of melting with temperature increasing from the solidus to the liquidus and a small decrease with pressure from ~6% to ~4% from 30 to 130 GPa, respectively. This significantly positive value of $\Delta V_m/V_{Bg}$ should contribute to a positive melt buoyancy for all types of melts.

5.3. Liquid-solid Fe partitioning

Based on LVP experiments performed up to ~35 GPa, Fe is recognized as an incompatible element, with a concentration ~1.5 to ~3 times higher in the melt compared to the solid mantle (e.g. (Ito et al., 2004; Liebske et al., 2005)). For samples recovered from LH-DAC experiments, Fe was reported to become extremely incompatible with the Bg structure at pressures above ~70 GPa, with a Fe concentration more than 10 times higher in the melt, compared to Bg (Nomura et al., 2011) (Figure 8). Such an enrichment of iron in melts (associated to a very low Fe-concentration in the residual Bg) favors their higher density relative to the solid residue, facilitating their sinking towards the CMB. In this previous study, olivine was used as a starting material and the absence of Al could have favored a relatively low $D_{Fe}^{Bg/melt}$ value (Wood and Rubie, 1996). Still, another study performed on an Al-bearing peridotitic composition using the same experimental methodology confirms the very low Fe-content in the residual Bg (Tateno et al., 2014). We note that the Al partition coefficient between Bg and melt ($D_{Al}^{Bg/melt}$), which was also reported to decrease significantly from 1.8 to 0.64 with increasing pressure from 34 to 88 GPa in the same study. On the other hand, much higher $D_{Fe}^{Bg/melt}$ values of 0.5-0.6 were reported for a chondritic-mantle starting material using *in situ* X-ray fluorescence spectroscopy (Andrault et al., 2012). These last results favor denser Bg grains and

buoyant melts. The controversy cannot arise from slight compositional differences between starting materials, especially between peridotitic and chondritic mantle compositions used in (Tateno et al., 2014) and (Andrault et al., 2012), respectively. It should be related to differences in experimental and/or analytical techniques.

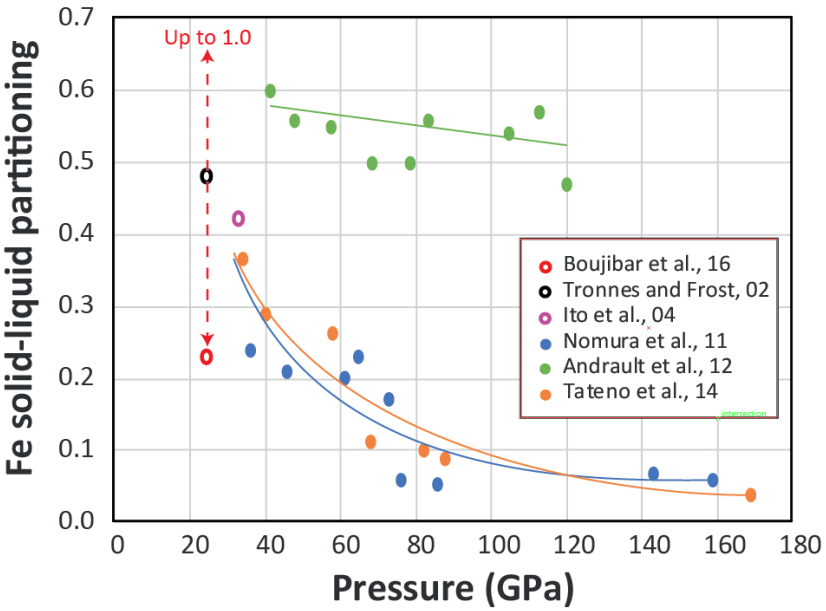

Figure 8: Change in Fe partitioning ($D_{Fe}^{Bg/melt}$) between the Bg and a coexisting melt. Starting materials for LH-DAC experiments were olivine (bleu, (Nomura et al., 2011)), chondritic-type mantle (green, (Andrault et al., 2012)) and peridotite (red, (Tateno et al., 2014)). Open circles correspond to previous multi-anvil experiments (Boujibar et al., 2016; Ito et al., 2004; Tronnes and Frost, 2002). The red arrow corresponds to the range of $D_{Fe}^{Bg/melt}$ measured in a same study at varying F values.

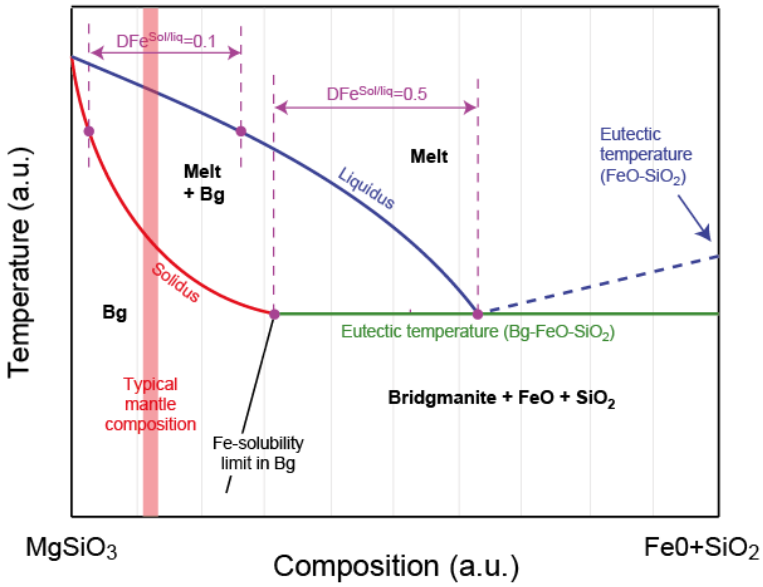

Figure 9: A possible, schematic, melting diagram between $MgSiO_3$ and $FeSiO_3$ in the lower mantle. We plot $FeO+SiO_2$ as the Fe-bearing end-member because $FeSiO_3$-Bg is unstable, except maybe at very high pressures. Vertical purple dashed lines are compositions of coexisting Bg and melt. Strong curvatures of solidus and liquidus lines can yield a decrease of $D_{Fe}^{Bg/melt}$ with increasing temperature between the eutectic and the liquidus temperature, in agreement with a previous study (Boujibar et al., 2016).

A recent study addresses the value of $D_{Fe}^{Bg/melt}$ as a function of F, the degree of partial melting, based on LVP experiments performed at ~25 GPa (Boujibar et al., 2016). $D_{Fe}^{Bg/melt}$ was found to vary from ~1 to a constant value of ~0.3, for F values below ~5 wt% or above 10 wt%, respectively. It suggests a $D_{Fe}^{Bg/melt}$ negatively correlated with temperature between the solidus and the liquidus, in agreement with a typical binary melting diagram (Figure 9). Thus, controversial results between previous LH-DAC experiments could arise from different heating conditions. Experiments reporting very low $D_{Fe}^{Bg/melt}$ values were performed using a very thin insulating material (hardly detectable using X-ray diffraction). A clear advantage is to facilitate the recovery of relatively thick samples, which can be cut after the experiment in order to obtain relatively large and homogeneous sample regions for chemical analyses using the electron microprobe. However, such experimental procedure implies strong axial temperature gradient between the two diamonds. The center part of the recovered samples is likely to correspond to relatively high temperatures, potentially close to the liquidus (high F possibly inducing low $D_{Fe}^{Bg/melt}$, Figure 9). Alternatively, experiments reporting higher $D_{Fe}^{Bg/melt}$

values used very thin samples well embedded in the insulating material (producing major diffraction peaks). While this type of loading minimizes axial temperature gradients in the sample, it makes the sample recovery much more difficult. In a previous study, X-ray diffraction was used to monitor carefully the onset of melting at the solidus temperature (Andrault et al., 2011) (low F possibly inducing high $D_{Fe}^{Bg/melt}$). Differences in heating procedure and thus in melting temperature between previous works could have induce significantly different values of $D_{Fe}^{Bg/melt}$. We note that the Fe behavior could be complicated by other factors: (i) the role of Al, which is not well constrained at high pressures; Due to the strong Al-Fe coupling in the Bg structure, an Al-depletion from the Bg structure would contribute to lower $D_{Fe}^{Bg/melt}$; (ii) the variable Fe^{2+} and Fe^{3+} fractions, because each one could partition differently between Bg and the melt, etc. Needless to say that a full quantitative model of $D_{Fe}^{Bg/melt}$ at lower mantle conditions requires additional experimental and theoretical studies.

5.4. SOLID-LIQUID DENSITY CONTRAST

The $\Delta\rho_{m-s}$ can be evaluated based on the density of both phases. All calculations were performed for a bulk mantle of pyrolitic composition. We consider a bulk Fe/(Mg+Fe) ratio (Fe#) of 0.1. We adjust the Fe-contents in the solid and the melt in order to reproduce the bulk mantle Fe-content, for various values of $D_{Fe}^{Bg/melt}$, which remains an adjustable parameter in the calculation. For the coexisting solid and melt compositions, we first calculate the densities in the solid state, before we apply a correction to the melt density of 6% to 4% for pressures between 30 and 130 GPa, respectively, to take into account the volume of melting (Figure 2). Composition of the solid can correspond either to (i) pure Bg, as expected for the residual solid from solidus to liquidus temperatures in our pseudo-binary melting diagrams (Figure 4), or to (ii) the mineral assemblage typical of pyrolite, which would correspond to the mantle composition in case of incipient melting. On the other hand, composition of the melt is approximated by a mixture of 55% Bg, 6.2 % CaPv and 38.8 % Fp, which represents well the PE-melt at all lower mantle pressures (Figure 4). We neglect the P-T dependence of melt composition, because the $X(SiO_2)$ value of the PET is not very different from the bulk pyrolitic mantle. Densities at high P and T of each phases are calculated based on their respective molar fractions of the following five different end-members: Al-bearing $MgSiO_3$, $FeSiO_3$, MgO, FeO, CaPv, using the PVT equation of state of each of them. We used the Mie-Grüneisen formalism with an auto-coherent set of elastic parameters (Matas et al., 2007).

Our calculation shows that the degree of partial melting has a major effect on melting properties (Figure 10). It affects (i) the Bg-content (and thus $X(SiO_2)$) in the melt, which increases moderately with temperature from PET to the liquidus (Figure 4), (ii) potentially the $D_{Fe}^{Bg/melt}$ value ((Boujibar et al., 2016); Figure 9) and (iii) Fe-contents in coexisting solid and melt, which vary with F independently from $D_{Fe}^{Bg/melt}$. In the context of mantle partial melting, two end-member situations arise:

A) During the first stages of magma ocean crystallization, F values are expected to be large. They could range between ~0.6 to 1, which corresponds to temperatures between the PET and the liquidus (Figure 6). We also note the threshold F value of ~0.4 corresponding to point when the magma ocean becomes more viscous (Abe, 1997). The situation corresponds to a variable fraction of Bg grains entrained in a major amount of melt. Close to the liquidus (F~1), Fe# in Bg could vary from ~0.05 to ~0.01, depending on the controversial values of $D_{Fe}^{Bg/Melt}$ from 0.5 to 0.1, respectively, because the Fe# in the melt is ~0.1, similar to the bulk mantle. Using the procedure described above, we calculate $\Delta\rho_{m-s}$ between coexisting Bg and pyrolitic melt along melting curves and obtain mostly negative values, meaning a relatively denser Bg grains (Figure 10). The value of $\Delta\rho_{m-s}$ increases with pressure,

due to a smaller volume of fusion at higher pressures but remains negative at all pressures from 30 to 135 GPa. $\Delta\rho_{m\text{-}s}$ also increases with decreasing the melt fraction, because the melt Fe# increases faster than the solid Fe#. We find no solid-melt density crossover for $D_{Fe}^{Bg/Melt}$ =0.5, at least for F values higher than 0.4. For $D_{Fe}^{Bg/Melt}$ =0.1, Bg can become less dense than the melt for F values below ~0.7.

B) At the latest stages of magma ocean crystallization, as well as in the context of partial melting in the present-day lower mantle, the situation corresponds to a minor amount of melt trapped in the solid mantle. The solid phase can be Bg or pyrolite, depending on the melting degree, F. Here, we report $\Delta\rho_{m\text{-}s}$ values corresponding to a solid phase made of pure Bg, however, results are not very different for pyrolite. Due to the lack of constraints, we assume a melt with $X(SiO_2)$ equal to that of the PE-melt, even if the situation could correspond to incipient mantle melting below the PET (low

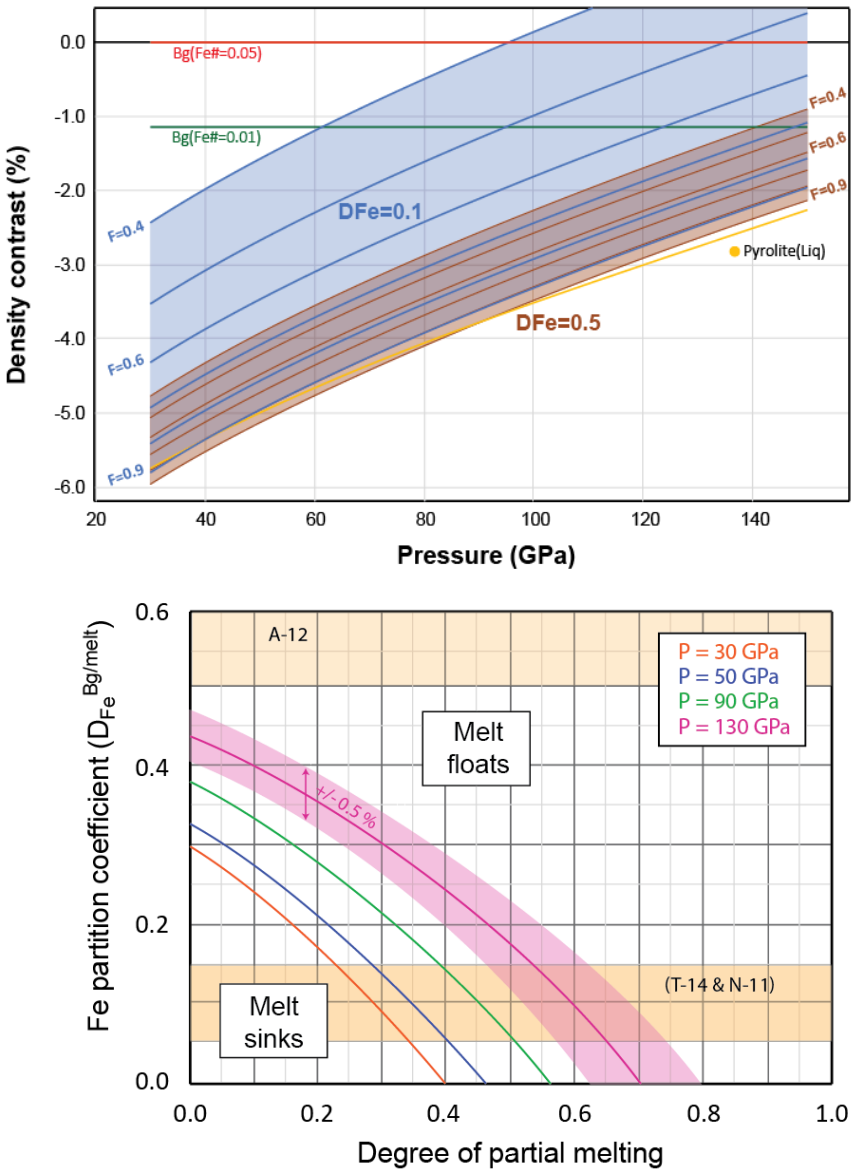

Figure 10: Density contrast for various couples of coexisting melt and Bg, in the context of a crystallizing magma ocean (F higher than 0.4). All values are normalized to the density of a same Bg having an Fe# of 5% (red). Negative values correspond to buoyant melt. We report relative densities of Bg with Fe# of 1% (green), fully molten pyrolite (yellow) and partial melts calculated for F values from 0.9 to 0.4. We perform the calculation for $D_{Fe}^{Bg/melt}$ values of 0.1 (blue area, corresponding to (Nomura et al., 2011; Tateno et al., 2014)) and 0.5 (brown area, corresponding to

Figure 11: Domains of positive or negative melt buoyancy for varying degrees of mantle partial melting and various possible values of the solid-liquid Fe partition coefficient. We report boundaries between "sink" and "float" domains at pressures of 30, 50, 90 and 130 GPa. The pink shaded region corresponds to a density contrast within 0.5%. Horizontal orange shaded regions correspond to ranges of $D_{Fe}^{Bg/melt}$ reported around 0.1 (T-14 & N-11; (Nomura et al., 2011; Tateno et al., 2014)) and 0.5 (A-12; (Andrault et al., 2012)) at high mantle depths (Figure 8).

F). Under these assumptions, the major change in melt composition with decreasing F is a higher Fe#. Calculations show that a denser melt, compared to a bridgmanitic mantle, is favored for (i) lower $D_{Fe}^{Bg/Melt}$, (ii) lower F and (iii) higher pressures (Figure 11). There is a significant range of parameters, for values of F below 0.7 and $D_{Fe}^{Bg/Melt}$ below 0.45, where melts could sink in the solid mantle toward the CMB. We remind here that the possible increase of $D_{Fe}^{Bg/Melt}$ at low F values (Boujibar et al., 2016) would favor buoyant melts.

6. Implications for crystallization of the Magma Ocean

6.1. Dynamics of the magma ocean crystallization

The crystallization of the early magma ocean is the primary mechanism invoked to produce a chemical stratification of the mantle (Boyet and Carlson, 2005; Caro et al., 2005). Concerning the mantle depth at which the crystallization began, our model suggests a mantle liquidus increasing smoothly with pressure up to the CMB pressure of 135 GPa (i.e. the A-chondritic model in Figure 1). Thus, the adiabatic temperature profile of the cooling magma ocean, which also presents a relatively constant slope, would likely cross the liquidus starting from the CMB upwards (e.g. Figure 7a in (Thomas and Asimow, 2013)). Magma ocean solidification should therefore occur from bottom up. We note that major changes in the dynamics of the magma ocean should occur at F values lower than ~40%, the critical melt fraction when the mantle becomes more viscous (Abe, 1997), rather than when the adiabatic profile crosses the liquidus (Monteux et al., 2016).

It has been proposed that Bg grains could settle in the magma ocean, inducing rejection of melts toward the Earth's surface (Boukare et al., 2015; Solomatov, 2007). Our calculations confirm a Bg denser than the coexisting melt at F values higher than 0.7 (Figure 11). Still, the effective gravitational segregation of Bg grains in a crystallizing magma ocean is not obvious. Highly turbulent flows have certainly dominated in the molten mantle. $\Delta\rho_{m\text{-}s}$ may not have been be sufficiently high to counterbalance mixing forces, especially in the lowermost mantle where $\Delta\rho_{m\text{-}s}$ decreases. This could have prevented major chemical segregation until late stages of the magma ocean crystallization. On the other hand, while an abrupt change in rheological behavior at F~40% should disable turbulent mixing flows, it should also slow down chemical segregation by inhibiting the atomic diffusion. Thus, the two side-effects of crystallization, turbulent flow followed by high mantle viscosity, are not in favor of large scale chemical heterogeneities early in the crystallizing Earth's mantle.

Following the assumption that Bg grains have efficiently segregated from the crystallizing magma ocean, the melt composition should drift toward higher Fe#, because Fe enters preferentially into the melt (e.g. (Boukare et al., 2015)) and also to a slightly higher SiO_2-content (due to the composition of the PET melt, Figure 5). Increasing the Fe# in melt favors higher $\Delta\rho_{m\text{-}s}$ and sinking melts. This effect could have contributed to produce an early BMO (Labrosse et al., 2007) and/or overturns (Elkins-Tanton, 2008). However, our melting model suggests that the Fe-enrichment of the melt could remain moderate. If we consider the most extreme case of (i) full gravitational segregation of the crystallizing Bg grains, (ii) a $D_{Fe}^{Sol/liq}$ value close to 0 and (iii) a bulk fractional crystallization of 60% (thus F=0.4), we find that the melt would reach Fe# of ~0.25 (for a bulk pyrolitic mantle with Fe# of ~0.1). For more reasonable sets of parameters, a high degree of Fe-enrichment can only occur at the very final stages of the magma ocean crystallization.

6.2. Chemical similarities between the Pseudo Eutectic-melt and peridotite

Major consequences arise from the very high F values found at the PET (Figure 6). Brutal solidification of the magma ocean could occur when the degree of partial melting becomes lower than 83% (for peridotite), 74% (for pyrolite) or 56% (for chondritic mantle) at a given mantle depth. Such F values are significantly higher than the threshold value of 40% necessary to produce a relatively viscous mantle (Abe, 1997). Therefore, final mantle crystallization could be achieved at the same time as the mantle became viscous. It would disable chemical segregation by melt gravitation in a mushy mantle and favor instead a homogeneous mantle after bulk magma ocean crystallization. Mantle

overturn would also be unlikely, because the magma ocean would crystallize before a too significant Fe-enrichment of the melt.

Our model shows that the peridotite composition is close to the PE-melt at high pressure (Figures 3 to 6). This compositional similarity was already discussed a long time ago (e.g. (Zhang and Herzberg, 1994)). This situation could result from a large scale chemical differentiation during magma ocean crystallization, where the upper part of the mantle would correspond to the last melt that solidified, and the residual solid, Bg, would be concentrated in the deep mantle. A floating layer of peridotitic melt of several hundred kilometers thickness (possibly even more than 1000 km) would have crystallized as a bulk, in agreement with our high F values at the PET. A highly bridgmanitic deep lower mantle would agree with previous studies (Matas et al., 2007; Murakami et al., 2012; Samuel et al., 2005).

Today, presence of volatile elements could induce incipient partial melting in the deep mantle. The melt could be denser than the mantle and sink, in the case the value of $D_{Fe}^{Bg/melt}$ would indeed be as low as 0.4, as suggested by some previous studies (Nomura et al., 2011; Tateno et al., 2014). Sinking melts could produce the ULVZ in the lowermost mantle, independently from the temperature prevailing in the lowermost mantle early in Earth's history. This scenario contrasts with another one suggesting that the ULVZ are the relic of an ancient BMO (Labrosse et al., 2007).

6.3. Maximum core temperature after magma ocean crystallization

After the Moon forming giant impact, the Earth has been largely molten. Subsequent cooling of the magma ocean could have been relatively fast, within 100 ky (Abe, 1997; Monteux et al., 2016; Solomatov, 2007). It was proposed that a BMO could have persisted in the lowermost mantle for a much longer time, due to a large amount of heat stored in the core (Labrosse et al., 2007). Still, the early temperature of the CMB (a good proxy for the core temperature), as well as the lifetime of the BMO remain highly debated. To keep a hot BMO thermally stable, there must be a layer of solid material just above it producing an efficient thermal blanketing between the molten BMO in contact with the hot core and the solid mantle. This solid shell would hamper escape of the core heat. This solid material could only be Bg, the liquidus phase in the deep mantle. Consequently, the Bg melting point of ~5400 K at a pressure of 135 GPa (Figure 1) corresponds formally to the highest possible CMB temperature after crystallization of the magma ocean. It is ~1300 K above the current CMB temperature.

However, a temperature of ~5400 K represents an improbable upper limit for the early CMB temperature. Indeed, the physical contact between the BMO and the overlaying Bg layer can react chemically. The further away from Bg is the chemical composition of the BMO, the lower should be the equilibrium temperature, in agreement with binary phase diagrams (Figure 4). And the more likely the CMB temperature after magma ocean crystallization could correspond to the first occurrence of a more viscous mantle at the CMB (Monteux et al., 2016). This temperature is estimated to ~4400 K, only ~300 K higher than the CMB temperature today (Andrault et al., 2016).

Acknowledgments: This work has been supported by the ANR contract "OxyDeep". This research was financed by the French Government Laboratory of Excellence initiative n°ANR-10-LABX-0006, the Région Auvergne and the European Regional Development Fund. This is Laboratory of Excellence ClerVolc contribution number XX.

References:

Abe, Y., 1997. Thermal and chemical evolution of the terrestrial magma ocean. Phys. Earth Planet. Inter. 100, 27-39.

Agee, C.B., 1998. Crystal-liquid density inversions in terrestrial and lunar magmas. Phys. Earth Planet. Inter. 107, 63-74.

Akaogi, M., Ito, E., 1999. Calorimetric study on majorite-perovskite transition in the system $Mg_4Si_4O_{12}$-$Mg_3Al_2Si_3O_{12}$: transition boundaries with positive pressure-temperature slopes. Phys. Earth Planet. Inter. 114, 129-140.

Akins, J.A., Luo, S.N., Asimow, P.D., Ahrens, T.J., 2004. Shock-induced melting of $MgSiO_3$ perovskite and implications for melts in Earth's lowermost mantle. Geophys. Res. Lett. 31, L14612.

Andrault, D., Bolfan-Casanova, N., Bouhifd, M.A., Guignot, N., Kawamoto, T., 2007. The role of Al-defects on the equation of state of Al-(Mg,Fe)SiO3 perovskite. Earth Planet. Sci. Lett. 263, 167-179.

Andrault, D., Bolfan-Casanova, N., Lo Nigro, G., Bouhifd, M.A., Garbarino, G., Mezouar, M., 2011. Melting curve of the deep mantle applied to properties of early magma ocean and actual core-mantle boundary. Earth Planet. Sci. Lett. 304, 251-259.

Andrault, D., Monteux, J., Le Bars, M., Samuel, H., 2016. The deep Earth may not be cooling down. Earth Planet. Sci. Lett. 443, 195-203.

Andrault, D., Pesce, G., Bouhifd, M.A., Bolfan-Casanova, N., Henot, J.M., Mezouar, M., 2014. Melting of subducted basalt at the core-mantle boundary. Science 344, 892-895.

Andrault, D., Petitgirard, S., Lo Nigro, G., Devidal, J.L., Veronesi, G., Garbarino, G., Mezouar, M., 2012. Solid-liquid iron partitioning in Earth's deep mantle. Nature 487, 354-357.

Bajgain, S., Ghosh, D.B., Karki, B.B., 2015. Structure and density of basaltic melts at mantle conditions from first-principles simulations. Nature Communications 6.

Benmore, C.J., Soignard, E., Amin, S.A., Guthrie, M., Shastri, S.D., Lee, P.L., Yarger, J.L., 2010. Structural and topological changes in silica glass at pressure. Phys. Rev. B 81.

Bolfan-Casanova, N., Keppler, H., Rubie, D.C., 2003. Water partitioning at 660 km depth and evidence for very low water solubility in magnesium silicate perovskite. Geophys. Res. Lett. 30, L017182.

Boujibar, A., Bolfan-Casanova, N., Andrault, D., Bouhifd, M.A., Trcera, N., 2016. Incorporation of Fe^{2+} and Fe^{3+} in bridgmanite during magma ocean crystallization. Am. Miner. 101, 1560-1570.

Boukare, C.E., Ricard, Y., Fiquet, G., 2015. Thermodynamics of the MgO-FeO-SiO2 system up to 140GPa: Application to the crystallization of Earth's magma ocean. J. Geophys. Res.: Solid Earth 120, 6085-6101.

Boyet, M., Carlson, R.W., 2005. Nd-142 evidence for early (> 4.53 Ga) global differentiation of the silicate Earth. Science 309, 576-581.

Caro, G., Bourdon, B., Wood, B.J., Corgne, A., 2005. Trace-element fractionation in Hadean mantle generated by melt segregation from a magma ocean. Nature 436, 246-249.

Corgne, A., Liebske, C., Wood, B.J., Rubie, D.C., Frost, D.J., 2005. Silicate perovskite-melt partitioning of trace elements and geochemical signature of a deep perovskitic reservoir. Geochim. Cosmochim. Acta 69, 485-496.

Davaille, A., 1999. A simultaneous generation of hotpots and superswells by convection in a heterogeneous planetary mantle. Nature 402, 756-760.

Davies, C., Pozzo, M., Gubbins, D., Alfe, D., 2015. Constraints from material properties on the dynamics and evolution of Earth's core. Nat. Geosci. 8, 678-+.

de Koker, N., Karki, B.B., Stixrude, L., 2013. Thermodynamics of the MgO-SiO_2 liquid system in Earth's lowermost mantle from first principles. Earth Planet. Sci. Lett. 361, 58-63.

de Koker, N., Stixrude, L., 2009. Self-consistent thermodynamic description of silicate liquids, with application to shock melting of MgO periclase and $MgSiO_3$ perovskite. Geophys. J. Int. 178, 162-179.

Du, Z., Lee, K.K.M., 2014. High-pressure melting of MgO from (Mg,Fe)O solid solutions. Geophys. Res. Lett. 41, 8061-8066.

Elkins-Tanton, L.T., 2008. Linked magma ocean solidification and atmospheric growth for Earth and Mars. Earth Planet. Sci. Lett. 271, 181-191.

Fiquet, G., Auzende, A.L., Siebert, J., Corgne, A., Bureau, H., Ozawa, H., Garbarino, G., 2010. Melting of Peridotite to 140 Gigapascals. Science 329, 1516-1518.
Funamori, N., Sato, T., 2010. Density contrast between silicate melts and crystals in the deep mantle: An integrated view based on static-compression data. Earth Planet. Sci. Lett. 295, 435-440.
Guillot, B., Sator, N., 2007. A computer simulation study of natural silicate melts. Part II: High pressure properties. Geochim. Cosmochim. Acta 71, 4538-4556.
Herzberg, C., Asimow, P.D., Ionov, D.A., Vidito, C., Jackson, M.G., Geist, D., 2013. Nickel and helium evidence for melt above the core-mantle boundary. Nature 493, 393-U134.
Herzberg, C., Condie, K., Korenaga, J., 2010. Thermal history of the Earth and its petrological expression. Earth Planet. Sci. Lett. 292, 79-88.
Herzberg, C., Zhang, J.Z., 1998. Melting experiments in the systems CaO-MgO-Al2O3-SiO2 and MgO-SiO2 at 3 to 15 GPa. Am. Miner. 83, 491-500.
Hirschmann, M.M., Asimow, P.D., Ghiorso, M.S., Stolper, E.M., 1999. Calculation of peridotite partial melting from thermodynamic models of minerals and melts. III. Controls on isobaric melt production and the effect of water on melt production. Journal of Petrology 40, 831-851.
Irifune, T., Koizumi, T., Ando, J., 1996. An experimental study of the garnet-perovskite transformation in the system MgSiO3-Mg3Al2Si3O12. Phys. Earth Planet. Inter. 96, 147-157.
Ito, E., Kubo, A., Katsura, T., Walter, M.J., 2004. Melting experiments of mantle materials under lower mantle conditions with implications for magma ocean differentiation. Phys. Earth Planet. Inter. 143-144, 397-406.
Katsura, T., Ito, E., 1990. Melting and subsolidus phase-relations in the $MgSiO_3$-$MgCO_3$- system at high-pressures - Implications to the evoluionj of the Earth's atmosphere. Earth Planet. Sci. Lett. 99, 110-117.
Katsura, T., Yoneda, A., Yamazaki, D., Yoshino, T., Ito, E., 2010. Adiabatic temperature profile in the mantle. Phys. Earth Planet. Inter. 183, 212-218.
Kellogg, L.H., Hager, B.H., van der Hilst, R.D., 1999. Compositional Stratification in the Deep Mantle. Science 283, 1881-1884.
Kojitani, H., Akaogi, M., 1997. Melting enthalpies of mantle peridotite: calorimetric determinations in the system CaO-MgO-Al2O3-SiO2 and application to magma generation. Earth Planet. Sci. Lett. 153, 209-222.
Labrosse, S., 2015. Thermal evolution of the core with a high thermal conductivity. Phys. Earth Planet. Inter. 247, 36-55.
Labrosse, S., Hernlund, J.W., Coltice, N., 2007. A crystallizing dense magma ocean at the base of the Earth's mantle. Nature 450, 866-869.
Lange, R.A., 1997. A revised model for the density and thermal expansivity of K_2O-Na_2O-CaO-MgO-Al_2O_3-SiO_2 liquids from 700 to 1900 K: extension to crustal magmatic temperatures. Contributions to Mineralogy and Petrology 130, 1-11.
Lauterbach, S., McCammon, C.A., van Aken, P., Langenhorst, F., Seifert, F., 2000. Mössbauer and ELNES spectroscopy of (Mg,Fe)(Si,Al)O3 perovskite: a highly oxidized component of the lower mantle. Contribution in Mineralogy and Petrology 138, 17-26.
Lebrun, T., Massol, H., Chassefiere, E., Davaille, A., Marcq, E., Sarda, P., Leblanc, F., Brandeis, G., 2013. Thermal evolution of an early magma ocean in interaction with the atmosphere. J. Geophys. Res.: Planets 118, 1155-1176.
Lee, C.-T.A., Luffi, P., Hoink, T., Li, J., Dasgupta, R., Hernlund, J.W., 2010. Upside-down differentiation and generation of a "primordial" lower mantle. Nature 463, 930-933.
Liebske, C., Corgne, A., Frost, D.J., Rubie, D.C., Wood, B.J., 2005. Compositional effects on element partitioning between Mg-silicate perovskite and silicate melts. Contrib. Mineral. Petrol. 149.
Liebske, C., Frost, D.J., 2012. Melting phase relations in the MgO-$MgSiO_3$ system between 16 and 26 GPa: Implications for melting in Earth's deep interior. Earth Planet. Sci. Lett. 345, 159-170.
Litasov, K., Ohtani, E., 2002. Phase relations and melt compositions in CMAS–pyrolite–H2O system up to 25 GPa. Phys. Earth Planet. Inter. 134, 105-127.
Mao, W.L., Meng, Y., Shen, G., Prakapenka, V.B., Campbell, A.J., Heinz, D.L., Shu, J., Caracas, R., Cohen, R.E., Fei, Y., Hemley, R.J., Mao, H.K., 2005. Iron-rich silicate in the Earth's D" layer. Proc. Natl. Acad. Sci. U. S. A. 102, 9751–9753.
Martin, H., Moyen, J.F., 2002. Secular changes in tonalite-trondhjemite-granodiorite composition as markers of the progressive cooling of Earth. Geology 30, 319-322.
Matas, J., Bass, J.D., Ricard, Y., Mattern, E., Bukowinsky, M.S., 2007. On the bulk composition of the lower mantle: predictions and limitations from generalized inversion of radial seismic profiles. Geophys. J. Int. 170, 764-780.

Matsukage, K.N., Jing, Z.C., Karato, S., 2005. Density of hydrous silicate melt at the conditions of Earth's deep upper mantle. Nature 438, 488-491.
Miller, G.H., Stolper, E.M., Ahrens, T.J., 1991. The Equation of State of a Molten Komatiite 2. Application to Komatiite Petrogenesis and the Hadean Mantle. J. Geophys. Res. 96, 11,849-811,864.
Monteux, J., Andrault, D., Samuel, H., 2016. On the cooling of a deep terrestrial magma ocean. Earth Planet. Sci. Lett. 448, 140-149.
Mosenfelder, J.L., Asimow, P.D., Frost, D.J., Rubie, D.C., Ahrens, T.J., 2009. The $MgSiO_3$ system at high pressure: Thermodynamic properties of perovskite, postperovskite, and melt from global inversion of shock and static compression data. J. Geophys. Res.: Solid Earth 114, B01203.
Mukhopadhyay, S., 2012. Early differentiation and volatile accretion recorded in deep-mantle neon and xenon. Nature 486, 101-U124.
Murakami, M., Ohishi, Y., Hirao, N., Hirose, K., 2012. A perovskitic lower mantle inferred from high-pressure, high-temperature sound velocity data. Nature 485, 90-U118.
Nakagawa, T., Tackley, P.J., 2010. Influence of initial CMB temperature and other parameters on the thermal evolution of Earth's core resulting from thermochemical spherical mantle convection. Geochem., Geophys., Geosyst. 11, Q06001.
Nakajima, M., Stevenson, D.J., 2015. Melting and Mixing States of the Earth's Mantle after the Moon-Forming Impact. Earth Planet. Sci. Lett., in press.
Nomura, R., Hirose, K., Uesugi, K., Ohishi, Y., Tsuchiyama, A., Miyake, A., Ueno, Y., 2014. Low Core-Mantle Boundary Temperature Inferred from the Solidus of Pyrolite. Science 343, 522-525.
Nomura, R., Ozawa, H., Tateno, S., Hirose, K., Hernlund, J.W., Muto, S., Ishii, H., Hiraoka, N., 2011. Spin crossover and iron-rich silicate melt in the Earth's deep mantle. Nature 473, 199-202.
Panero, W.R., Pigott, J.S., Reaman, D.M., Kabbes, J.E., Liu, Z.X., 2015. Dry (Mg,Fe)SiO3 perovskite in the Earth's lower mantle. J. Geophys. Res.: Solid Earth 120, 894-908.
Petitgirard, S., Malfait, W.J., Sinmyo, R., Kupenko, I., Hennet, L., Harries, D., Dane, T., Burghammer, M., Rubie, D.C., 2015. Fate of MgSiO3 melts at core–mantle boundary conditions. Proceedings of the National Academy of Sciences 112, 14186-14190.
Presnall, D.C., 1995. Phase diagrams of Earth-forming minerals, in: Ahrens, T. (Ed.), Mineral Physics and Crystallography. AGU, Washington, D.C, pp. 248-268.
Presnall, D.C., Gasparik, T., 1990. Melting of enstatite ($MgSiO_3$) from 10 to 16.5 GPa and the forsterite (Mg_2SiO_4) - majorite ($MgSiO_3$) eutectic at 16.5 GPa - Implications for the origin of the mantle. J. Geophys. Res. 95, 15771-15777.
Revenaugh, J., Sipkin, S.A., 1994. Seismic evidence for silicate melt atop the 410 km mantle discontinuity. Nature 369, 474-476.
Romanowicz, B., 1995. A global tomographic model of the shear attenuation in the upper mantle. J. Geophys. Res.: Solid Earth 100, 12375-12394.
Rost, S., Garnero, E.J., Williams, Q., Manga, M., 2005. Seismological constraints on a possible plume root at the core-mantle boundary. Nature 435, 666-669.
Rubie, D.C., Nimmo, H.J., Melosh, H.J., 2015. Formation of the Earth's core, in: Schubert, G. (Ed.), Treatise on Geophysics, 2 ed. Elsevier, Amsterdam, pp. 43-79.
Sakamaki, T., Suzuki, A., Ohtani, E., 2006. Stability of hydrous melt at the base of the Earth's upper mantle. Nature 439, 192-194.
Samuel, H., Farnetani, C.G., Andrault, D., 2005. Heterogeneous lowermost mantle: Compositional constraints and seismological observables, in: VanDerHilst, R.D., Bass, J.D., Matas, J., Trampert, J. (Eds.), Earth's Deep Mantle: Structure, Composition, and Evolution, pp. 101-116.
Sanloup, C., Drewitt, J.W.E., Konopkova, Z., Dalladay-Simpson, P., Morton, D.M., Rai, N., van Westrenen, W., Morgenroth, W., 2013. Structural change in molten basalt at deep mantle conditions. Nature 503, 104-+.
Sato, T., Funamori, N., 2010. High-pressure structural transformation of SiO2 glass up to 100 GPa. Phys. Rev. B 82.
Shen, G., Lazor, P., 1995. Measurement of melting temperatures of some minerals under lower mantle conditions. J. Geophys. Res. 100, 17699-17713.
Simon, F., Glatzel, G., 1929. Fusion-pressure curve. Zeitschrift für anorganische und allgemeine Chemie 178, 309-316.
Sleep, N.H., Zahnle, K.J., Lupu, R.E., 2014. Terrestrial aftermath of the Moon-forming impact. Philos. Trans. R. Soc., A 372.
Solomatov, V.S., 2007. Magma Oceans and Primordial Mantle Differentiation, in: Schubert, G. (Ed.), Treatise on Geophysics. Elsevier, Amsterdam, pp. 91-119.

Song, T.R.A., Helmberger, D.V., Grand, S.P., 2004. Low-velocity zone atop the 410-km seismic discontinuity in the northwestern United States. Nature 427, 530-533.
Stebbins, J.F., Carmichael, I.S.E., Moret, L.K., 1984. Heat-capacities and entropies of silicate liquids and glasses. Contributions to Mineralogy and Petrology 86, 131-148.
Stixrude, L., de Koker, N., Sun, N., Mookherjee, M., Karki, B.B., 2009. Thermodynamics of silicate liquids in the deep Earth. Earth Planet. Sci. Lett. 278, 226-232.
Stixrude, L., Karki, B.B., 2005. Structure and freezing of $MgSiO_3$ liquid in the Earth's lower mantle. Science 310, 297-299.
Stolper, E.M., Ahrens, T.J., 1987. On the nature of pressure induced coordination changes in silicate melts or glasses. Geophys. Res. Lett. 14, 1231-1233.
Tateno, S., Hirose, K., Ohishi, Y., 2014. Melting experiments on peridotite to lowermost mantle conditions. J. Geophys. Res.: Solid Earth 119, 4684-4694.
Tauzin, B., Debayle, E., Wittlinger, G., 2010. Seismic evidence for a global low-velocity layer within the Earth's upper mantle. Nat. Geosci. 3, 718-721.
Thomas, C.W., Asimow, P.D., 2013. Direct shock compression experiments on premolten forsterite and progress toward a consistent high-pressure equation of state for CaO-MgO-Al2O3-SiO2-FeO liquids. J. Geophys. Res.: Solid Earth 118, 5738-5752.
Thomas, C.W., Liu, Q., Agee, C.B., Asimow, P.D., Lange, R.A., 2012. Multi-technique equation of state for Fe2SiO4 melt and the density of Fe-bearing silicate melts from 0 to 161 GPa. J. Geophys. Res.: Solid Earth 117.
Thomson, A.R., Walter, M.J., Lord, O.T., Kohn, S.C., 2014. Experimental determination of melting in the systems enstatite-magnesite and magnesite-calcite from 15 to 80 GPa. Am. Miner. 99, 1544-1554.
Touboul, M., Puchtel, I.S., Walker, R.J., 2012. W-182 Evidence for Long-Term Preservation of Early Mantle Differentiation Products. Science 335, 1065-1069.
Tronnes, R.G., Frost, D.J., 2002. Peridotite melting and mineral–melt partitioning of major and minor elements at 22–24.5 GPa. Earth Planet. Sci. Lett. 197, 117-131.
van der Hilst, R.D., Karason, H., 1999. Compositional heterogeneity in the bottom 1000 kilometers of Earth's mantle: Toward a hybrid convection model. Science 283, 1885-1888.
Vocadlo, L., Price, G.D., 1996. The melting of MgO - Computer calculations via molecular dynamics. Physics and Chemistry of Minerals 23, 42-49.
Wang, Y.B., Sakamaki, T., Skinner, L.B., Jing, Z.C., Yu, T., Kono, Y., Park, C., Shen, G.Y., Rivers, M.L., Sutton, S.R., 2014. Atomistic insight into viscosity and density of silicate melts under pressure. Nature Communications 5.
Wicks, J.K., Jackson, J.M., Sturhahn, W., 2010. Very low sound velocities in iron-rich (Mg,Fe)O: Implications for the core-mantle boundary region. Geophys. Res. Lett. 37.
Wood, B.J., Rubie, D.C., 1996. The effect of alumina on phase transformations at the 660-kilometer discontinuity from Fe-Mg partitioning experiments. Science 273, 1522-1524.
Yu, Y.G., Wentzcovitch, R.M., Vinograd, V.L., Angel, R.J., 2011. Thermodynamic properties of $MgSiO_3$ majorite and phase transitions near 660 km depth in $MgSiO_3$ and Mg_2SiO_4: A first principles study. J. Geophys. Res.: Solid Earth 116.
Zeidler, A., Salmon, P.S., Skinner, L.B., 2014. Packing and the structural transformations in liquid and amorphous oxides from ambient to extreme conditions. Proc. Natl. Acad. Sci. U. S. A. 111, 10045-10048.
Zerr, A., Boehler, R., 1993. Melting of $(Mg,Fe)SiO_3$-perovskite to 625 kbar: Indication of a high melting temperature in the lower mantle. Science 262, 553–555.
Zhang, J., Herzberg, C., 1994. Melting experiments on anhydrous peridotite KLB-1 from 5.0 to 22.5 GPa. J. Geophys. Res. 99, 17729-17742.